

REPORT DOCUMENTATION PAGE

Form Approved
OMB No. 0704-0188

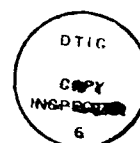
Public reporting burden for this collection of information is estimated to average 1 hour per response, including the time for reviewing instructions, searching existing data sources, gathering and maintaining the data needed, and completing and reviewing the collection of information. Send comments regarding this burden estimate or any other aspect of this collection of information, including suggestions for reducing this burden, to Washington Headquarters Services, Directorate for Information Operations and Reports, 1215 Jefferson Davis Highway, Suite 1204, Arlington, VA 22202-4302, and to the Office of Management and Budget, Paperwork Reduction Project (0704-0188), Washington, DC 20503.

1. Agency Use Only (Leave blank).		2. Report Date. 1990		3. Report Type and Dates Covered. Journal Article	
4. Title and Subtitle. An Operational Global-Scale Ocean Thermal Analysis System				5. Funding Numbers. Program Element No. 63704N Project No. Task No. Accession No. DN394457	
6. Author(s). R. Michael Clancy, Patricia A. Phoebe, and Kenneth D. Pollak				8. Performing Organization Report Number. JA 321:001:89	
7. Performing Organization Name(s) and Address(es). Naval Oceanographic and Atmospheric Research Laboratory Stennis Space Center, MS 39529-5004				10. Sponsoring/Monitoring Agency Report Number. JA 321:001:89	
9. Sponsoring/Monitoring Agency Name(s) and Address(es). Space and Naval Warfare Systems Command Washington, D.C.				11. Supplementary Notes. JAOT	
12a. Distribution/Availability Statement. Approved for public release; distribution is unlimited.				12b. Distribution Code.	
13. Abstract (Maximum 200 words). The optimum Thermal Interpolation System (OTIS) is an ocean thermal analysis product developed for real-time operational use at the U.S. Navy's Fleet Numerical Oceanography Center. It functions in an analysis-prediction-analysis data assimilation cycle with an ocean mixed-layer model using the optimum interpolation formulation of Alaka and Elvander (1972). Thus, climatology serves as the first-guess field for the analysis of synoptic ship, bathythermograph, buoy, and satellite data, with the prediction from the mixed-layer model treated as a special class of data. An operational test, involving comparisons of OTIS against an existing operational ocean thermal structure model, was conducted during February, March, and April 1988. Qualitative comparison of the two products with over 9900 independent (i.e., unassimilated) bathythermograph observations to calculate apparent root-mean-square (rms) errors indicate that OTIS gives a more accurate analysis of the thermal structure with improvements largest below the base of the mixed layer. Regional differences in the relative performance of the models which are probably related to the validity of the prescribed statistical parameters required by OTIS, are also noted from verification against the bathythermograph data. OTIS performs best relative to the existing model in the Indian Ocean, and poorest relative to this model in the eastern midlatitude Pacific. In the latter area, however, both models exhibit their lowest error levels and perform best relative to climatology. Subgrid-scale noise contaminates the apparent rms error statistics and obscures the relative grid-scale accuracy of the models. A general technique is presented to estimate grid-scale rms errors which are uncontaminated by subgrid-scale and instrumental noise in the observations. Application of the technique indicates that the grid-scale errors*					
14. Subject Terms. (U) Satellite SST; (U) Remote Sensing; (U) Thermodynamic Ocean Models; (U) Ocean Thermal Analysis; (U) Data Assimilation; (U) Ocean Thermal Structure; (U) Optimum Interpolation				15. Number of Pages. 22	
17. Security Classification of Report. Unclassified				16. Price Code.	
18. Security Classification of This Page. Unclassified		19. Security Classification of Abstract. Unclassified		20. Limitation of Abstract. SAR	

*errors for OTIS are typically 20% less than those of the other model.

OTIS was designated as the Navy's new operational global-scale ocean thermal analysis product in July 1988.

Accession For	
NTIS GRA&I	<input checked="checked" type="checkbox"/>
DTIC TAB	<input type="checkbox"/>
Unannounced	<input type="checkbox"/>
Justification	
By	
Distribution/	
Availability Codes	
Dist	Avail and/or Special
A-1	20



An Operational Global-Scale Ocean Thermal Analysis System

R. MICHAEL CLANCY

Ocean Models Division, Fleet Numerical Oceanography Center, Monterey, California

PATRICIA A. PHOEBUS*

Ocean Sensing and Prediction Division, Naval Ocean Research and Development Activity, John C. Stennis Space Center, Mississippi

KENNETH D. POLLAK

Ocean Models Division, Fleet Numerical Oceanography Center, Monterey, California

(Manuscript received 26 May 1989, in final form 5 September 1989)

ABSTRACT

The Optimum Thermal Interpolation System (OTIS) is an ocean thermal analysis product developed for real-time operational use at the U.S. Navy's Fleet Numerical Oceanography Center. It functions in an analysis-prediction-analysis data assimilation cycle with an ocean mixed-layer model using the optimum interpolation formulation of Alaka and Elvander (1972). Thus, climatology serves as the first-guess field for the analysis of synoptic ship, bathythermograph, buoy, and satellite data, with the prediction from the mixed-layer model treated as a special class of data.

An operational test, involving comparisons of OTIS against an existing operational ocean thermal structure model, was conducted during February, March, and April 1988. Qualitative comparison of the two products suggests that OTIS gives a more realistic representation of subsurface anomalies and horizontal gradients. Quantitative comparison of the two products with over 9900 independent (i.e., unassimilated) bathythermograph observations to calculate apparent root-mean-square (rms) errors indicate that OTIS gives a more accurate analysis of the thermal structure, with improvements largest below the base of the mixed layer. Regional differences in the relative performance of the models, which are probably related to the validity of the prescribed statistical parameters required by OTIS, are also noted from verification against the bathythermograph data. OTIS performs best relative to the existing model in the Indian Ocean, and poorest relative to this model in the eastern midlatitude Pacific. In the latter area, however, both models exhibit their lowest error levels and perform best relative to climatology.

Subgrid-scale noise contaminates the apparent rms error statistics and obscures the relative grid-scale accuracy of the models. A general technique is presented to estimate grid-scale rms errors which are uncontaminated by subgrid-scale and instrumental noise in the observations. Application of the technique indicates that the grid-scale errors for OTIS are typically 20% less than those of the other model.

OTIS was designated as the Navy's new operational global-scale ocean thermal analysis product in July 1988.

1. Introduction

Real-time monitoring of thermal structure in the upper ocean is becoming increasingly important as we seek a better understanding of global climate change. In addition, an accurate representation of the upper ocean is important in both long-range and medium-range weather prediction, fisheries management, and the operation of underwater acoustic systems. The U.S. Navy's Fleet Numerical Oceanography Center (FNOC), Monterey, California, has operated com-

puterized analyses for real-time monitoring of ocean thermal structure on global and regional scales for over 25 years. In general, these analyses have combined real-time ship, bathythermograph (bathy), buoy, and satellite observations with climatology and predictions from numerical ocean models to produce fully automated "nowcasts" of ocean thermal structure.

The Optimum Thermal Interpolation System (OTIS) is the latest ocean thermal analysis product developed for operational use at FNOC. OTIS is based on the Optimum Interpolation (OI) data assimilation technique of Gandin (1965), which is used widely in meteorology. The OI technique has been applied to oceanographic analysis for research applications by Bretherton et al. (1976), Freeland and Gould (1976), McWilliams (1976), White (1977), White and Bernstein (1979), Bernstein and White (1981), Clancy

* Present affiliation: Naval Oceanographic and Atmospheric Research Laboratory, Atmospheric Directorate, Monterey, California.

Corresponding author address: R. Michael Clancy, Code 42, Fleet Numerical Oceanography Center, Monterey, CA 93943.

90 12 18 135

(1983), Roemmich (1983), Robinson and Leslie (1985), McWilliams et al. (1986), Hua et al. (1986), Robinson et al. (1986), Cummings (1986), Carter and Robinson (1987), Robinson et al. (1987), and others. Because the OI technique is well suited for handling data-sparse areas and assimilating data with differing error characteristics, it is an attractive approach for operational ocean thermal analysis.

Basically and in general, the OI technique maps observations distributed nonuniformly in space and time to a uniformly gridded synoptic representation, or analysis, of the target field. As in most objective analysis techniques, the concept of *resolvable* versus *subgrid-scale* features is fundamental in OI. Resolvable features are those of spatial extent greater than twice the mesh length of the analysis grid, which are thus capable of being at least marginally represented by the grid. *Subgrid-scale* features are those with spatial extent less than twice the mesh length which, as a result, cannot be resolved by the grid. As far as the analysis is concerned, subgrid-scale features contribute to the error in the observations.

An OI analysis is constructed as a background or first-guess field plus anomalies relative to this field. In general, the anomaly at a particular gridpoint is given by a weighted combination of observed anomalies, with the space-time autocorrelation function for the resolvable anomalies governing which observations contribute. The OI technique provides the optimum weights applied to the observed anomalies such that the resulting analysis error will be minimized in a least-squares sense. The technique also provides an estimate of this error. The basic inputs to this process are the statistics defining both the resolvable and subgrid-scale variability of the target field about the background field and the instrumental error characteristics of the measurement system providing the observations.

In operational meteorological applications of the OI technique, the first-guess field for the analysis is given generally by a model prediction from the previous analysis. Climatology, the long-term mean state of the atmosphere, does not enter the process. For operational oceanographic applications, however, this is not a viable approach: the present generation of ocean thermal prediction models, the atmospheric forcing used to drive them, and the observational data base available to update them are simply not good enough, at least for global-scale application, to keep the evolving thermal fields "on track." Climatological ocean thermal structure, derived from historical data, must be used as a constraining factor. Consequently, OTIS follows the approach of Alaka and Elvander (1972) by using climatology as the first-guess field for the OI analysis and treating input from an ocean prediction model as a special class of data. The prediction model used by OTIS is the Thermodynamic Ocean Prediction System (TOPS) mixed-layer model described by Clancy and Pollak (1983).

The Expanded Ocean Thermal Structure (EOTS) analysis has been operational at FNOC for almost ten years (Clancy 1987). EOTS combines real-time ocean thermal observations with climatology via the Fields-by-Information-Blending (FIB) analysis technique (Holl et al. 1979) to produce a three-dimensional analysis or "nowcast" of ocean thermal structure. A number of operational EOTS runs are made daily at FNOC corresponding to various regions of high Navy interest. When coupled additionally in certain regions to the TOPS mixed-layer model in an analysis-prediction-analysis data assimilation cycle, the system is referred to as the TOPS-Coupled EOTS (TEOTS) analysis (Clancy and Pollak 1983; Martin et al. 1985). Thermal fields from EOTS and TEOTS are used to support FNOC acoustic predictions and transmitted to numerous users through a variety of communications links.

An operational test was conducted between 1 February and 30 April 1988 to establish OTIS as a valid replacement for the global-scale implementation of TEOTS. This involved qualitative comparison of thermal fields produced by OTIS with those produced by TEOTS, and quantitative verification of both models against independent bathy data. During the test, OTIS and TEOTS functioned on the same horizontal grids (the standard FNOC Northern Hemisphere and Southern Hemisphere 63×63 polar stereographic grids; see Clancy and Pollak 1983), used the same monthly ocean thermal climatology, functioned on the same schedule (one analysis per day), and had access to the same real-time data base (i.e., synoptic ship, buoy, bathy, and satellite observations). Throughout the test, OTIS was coupled with its own version of TOPS in an analysis-prediction-analysis data assimilation cycle independent of TEOTS. The TOPS mixed-layer model coupled with OTIS contained exactly the same physics and used exactly the same atmospheric forcing as that which was coupled to TEOTS.

The purpose of this paper is to document the techniques and assumptions used in OTIS, and present the results of the operational test of the global-scale OTIS at FNOC.

2. Description of the analysis procedure

In performing an analysis, OTIS proceeds point-by-point through its horizontal grid, producing a complete profile from the surface to the deepest analyzed level at each gridpoint before advancing to the next. At each of these gridpoints, the analysis sequence is 1) sea surface temperature, 2) temperature in the mixed layer, and 3) temperature below the mixed layer.

a. Sea surface temperature analysis

OTIS represents the analyzed sea surface temperature (SST) at the k th gridpoint T_k^s as

these data and tend to control their weighting relative to climatology, other data, and TOPS in the analysis.

The MCSST data are handled in a special way which complicates the determination of $(\sigma_i^n)_{\text{MCSST}}^2$. Before assimilation into the analysis, the MCSST reports within one-half mesh length of each gridpoint are block averaged around the gridpoint to form "super-observations" (see DiMego 1988) assumed valid at the gridpoint. Because high MCSST data densities usually result in many redundant MCSST reports around a gridpoint, this averaging process provides an efficient way to incorporate these high-resolution data without losing any information on the *resolvable* thermal field. Thus, if the i th observation in Eq. (1) is an MCSST observation, it is in fact given by

$$(T_i^n)_{\text{MCSST}} = \frac{1}{M} \sum_{j=1}^M \tau_j \quad (8)$$

where τ_j is the j th individual MCSST report and M is the total number of individual MCSST reports used in the block average. Thus, in view of Eq. (8), the expression for $(\sigma_i^n)_{\text{MCSST}}^2$ becomes

$$(\sigma_i^n)_{\text{MCSST}}^2 = \frac{1}{M} [\epsilon_{\text{MCSST}}^2 + (\sigma_i^n)^2 + (\sigma_i^r)^2] + e_{\text{MCSST}}^2 \quad (9)$$

where ϵ_{MCSST} and e_{MCSST} are the standard deviation and mean, respectively, of the instrumental error for the MCSST reports and σ_i^r is the standard deviation of the SST field resulting from resolvable SST variations over the domain in which the MCSST block averaging is done. The term $(\sigma_i^r)^2$ represents the variance added because the differencing of the MCSST data with climatology is done *after* the block averaging and with the climatological temperature valid at the gridpoint rather than *before* the block averaging and with temperatures obtained by interpolating climatology to each individual MCSST observation. This term is estimated by assuming a constant reference SST gradient and averaging the resulting temperature variance over one grid space. Thus,

$$(\sigma_i^r)^2 = \frac{(T' \Delta X)^2}{12} \quad (10)$$

where T' is a reference climatological SST gradient (taken to be $0.01^\circ\text{C km}^{-1}$) and ΔX is a reference grid space for the OTIS grid. Thus, for the FNOC 63×63 hemispheric grid ($\Delta X = 320$ km), $\sigma_i^r = 0.85^\circ\text{C}$.

No attempt is made to correct for any mean error (i.e., bias) in the MCSST data. Rather, e_{MCSST}^2 effectively becomes a lower bound on the MCSST observational error when M becomes large. The quantities ϵ_{MCSST} and e_{MCSST} are user-specified parameters which tend to control the relative weighting of the MCSST data in the analysis.

The value of the TOPS prediction rms error σ_k^p for use in Eq. (5) is obtained from

$$(\sigma_k^p)^2 = (\sigma_k^n)_{\text{INITIAL}}^2 + G_k^2 \quad (11)$$

where $(\sigma_k^n)_{\text{INITIAL}}$ is the rms error of the resolvable thermal field from the previous analysis initializing TOPS and G_k is the rms TOPS error growth over one analysis-prediction-analysis cycle (i.e., 24 hours). Thus, following the approach of Bengtsson and Gustafsson (1972), the error in the predicted thermal field is taken to be the error in the initial conditions plus the error added due to error growth in the prediction model. The quantity G is a user-specified parameter chosen to reflect the rate of error growth in TOPS. It tends to control the weight assigned to the TOPS prediction relative to climatology and observations.

Clancy et al. (1989) present idealized data assimilation studies to illustrate the behavior of the analysis-forecast-analysis coupling between OTIS and TOPS described above. In general, the mixed-layer model predictions reduce the error level of the analysis by accounting for the response of the upper ocean to local atmospheric forcing and carrying the integrated effect of this response forward in time. In the absence of large TOPS-predicted changes in the thermal structure and observational data to sustain OTIS-analyzed thermal anomalies, the thermal fields decay toward climatology at a rate which is governed by the prescribed TOPS error growth rate G_k .

The last user-specified parameter is the noise-to-signal ratio for the subgrid-scale error λ_i^n defined by

$$\lambda_i^n = \left[\frac{\sigma_i^n}{\sigma_i^c} \right]^2 \quad (12)$$

Like A , B , and C , this quantity must be chosen to reflect the statistics of ocean thermal variability. For example, λ_i^n must be larger in dynamically active regions, where subgrid-scale eddies produce large-amplitude but unresolved perturbations in the thermal field, than in more quiescent regions where the eddy field is weak. Of course, λ_i^n is a function of the grid mesh length, becoming smaller as the grid becomes finer and the unresolved portion of the thermal field decreases.

Equation (12) is used along with the rms difference between bathy observed temperatures and climatology σ_i^b to obtain σ_i^c and σ_i^n . Neglecting ϵ_{BATHY} , which is small compared to σ_i^n for the grid currently utilized by OTIS, and assuming that σ^c and σ^n are uncorrelated, $(\sigma_i^b)^2$ can be written

$$(\sigma_i^b)^2 = (\sigma_i^c)^2 + (\sigma_i^n)^2 \quad (13)$$

or just the sum of the mean-square resolvable signal about climatology plus the mean-square subgrid-scale noise. From (12) and (13),

$$(\sigma_i^c)^2 = \frac{(\sigma_i^b)^2}{1 + \lambda_i^n} \quad (14)$$

$$(\sigma_i^n)^2 = \frac{\lambda_i^n}{1 + \lambda_i^n} (\sigma_i^h)^2 \quad (15)$$

It is not possible to calculate $(\sigma_i^h)^2$ directly from the available real-time bathy data at every observational location simply because the bathy data coverage and observational density will not permit it. Therefore, $(\sigma_i^h)^2$ is estimated from

$$(\sigma_i^h)^2 = \frac{1 + \lambda_{at}^n}{1 + \lambda_{at}^n} (\sigma_{at}^h)^2 \quad (16)$$

where $(\sigma_{at}^h)^2$ is the mean-square departure of the bathy observations from climatology and λ_{at}^n is the average value of λ_i^n , both calculated over the entire analysis domain. The data used in this calculation consist of a running 60-day window of bathy observations reported to FNOC in real-time, amounting to about 9000 reports globally.

Using the assumption of Eq. (16), Eqs. (14) and (15) become

$$(\sigma_i^e)^2 = \frac{(\sigma_{at}^h)^2}{1 + \lambda_{at}^n} \quad (17)$$

$$(\sigma_i^n)^2 = \frac{\lambda_i^n}{1 + \lambda_{at}^n} (\sigma_{at}^h)^2 \quad (18)$$

With λ_i^n specified by the user, and σ_{at}^h and λ_{at}^n calculated internally by OTIS, Eqs. (17) and (18) provide σ_i^e and σ_i^n for use in Eqs. (4), (5), (6), (7), (9), and (12). Note that σ_{at}^h , and thus σ_i^e and σ_i^n , are determined separately for each standard level of the OTIS vertical output grid (see section 2b). Note also from Eq. (17) that σ_i^e is independent of horizontal location. Thus, implicit in Eq. (16) is the assumption that variations of the rms bathy error σ_i^h with location are produced entirely by variations in the rms subgrid-scale error σ_i^n .

Equations (2)–(12) and (17)–(18) constitute a closed set which can be solved for the weights α_{ki} and β_k . Once these weights are obtained, the analyzed temperature is calculated from Eq. (1). Also, the rms error of the resolvable thermal field σ_k^a can then be calculated from

$$(\sigma_k^a)^2 = (\sigma_k^e)^2 (1 + \beta_k + \sum_{i=1}^N \alpha_{ki} \eta_{ki}) \quad (19)$$

(see White and Bernstein 1979). Recognizing that OTIS initializes the TOPS forecast which will provide T_k^n for the following day's analysis, the value of $(\sigma_k^a)^2$ obtained from (19) becomes $(\sigma_k^a)^2_{\text{INITIAL}}$ of equation (11) (i.e., the error in the TOPS initial conditions) for the following day's analysis.

Finally, the expected departure of the thermal field from an independent bathy observation made precisely at the gridpoint at analysis time σ_k^v is given by

$$\sigma_k^v = [(\sigma_k^a)^2 + (\sigma_k^n)^2 + \epsilon_{\text{BATHY}}^2]^{0.5} \quad (20)$$

with the three terms inside the brackets representing the contributions of analysis error, subgrid-scale error, and instrumental error.

b. Mixed-layer analysis

Upon conclusion of the SST analysis at gridpoint k , OTIS performs an OI analysis for mixed-layer depth (MLD). In analogy to Eq. (1), the expression for the analyzed MLD h_k^a is

$$h_k^a = h_k^e + \sum_{i=1}^N \alpha_{ki} (h_i^n - h_i^e) + \beta_k (h_k^n - h_k^e) \quad (21)$$

where h_k^e is the climatological MLD at the gridpoint, h_k^n the predicted MLD at the gridpoint from the 24-hour TOPS forecast from the previous day's analysis, h_i^n the observed MLD at location i , h_i^e the climatological MLD at location i , α_{ki} the weight applied to the i th observed MLD anomaly $(h_i^n - h_i^e)$ assimilated at the gridpoint, β_k the weight applied to the TOPS predicted MLD anomaly $(h_k^n - h_k^e)$ at the gridpoint, and N the number of observations assimilated at the gridpoint.

The climatological MLD h_k^e is determined from examination of the climatological temperature profile, defined at gridpoint k on the OTIS vertical grid (see Table 1). Beginning at the surface and working downward, vertical temperature gradients are examined to find the shallowest pair of levels between which the vertical gradient is less than $-0.05^\circ\text{C m}^{-1}$. The layer depth h_k^e is then taken simply as the depth of the shallower level of this pair, and is thus always one of the discrete levels listed in Table 1. Exactly the same process is carried out on the TOPS and bathy profiles to define h_k^n and h_i^n . The TOPS-predicted profile is defined on the same vertical grid as OTIS, but the depths defining the bathy profiles are arbitrary, and thus the

TABLE 1. Vertical grid for OTIS output.

Level	Depth in meters
0	0.0
1	2.5
2	7.5
3	12.5
4	17.5
5	25.0
6	32.5
7	40.0
8	50.0
9	62.5
10	75.0
11	100.0
12	125.0
13	150.0
14	200.0
15	300.0
16	400.0

h_i'' 's generally fall somewhere in between the OTIS/TOPS fixed levels of Table 1.

The weights α_k and β_k in Eq. (21) are obtained by solving the $N + 1$ equations of (2) as before. In solving (2), the parameters η_{ij} , λ_i'' and λ_k'' are assumed proportional to the corresponding values for the temperature analysis at 100 m depth. This implies

$$(\sigma_i'')_{\text{MLD}} = (K)(\sigma_i'')_{100 \text{ m}} \quad (22)$$

$$(\sigma_k'')_{\text{MLD}} = (K)(\sigma_k'')_{100 \text{ m}} \quad (23)$$

$$(\sigma_k'')_{\text{MLD}} = (K)(\sigma_k'')_{100 \text{ m}} \quad (24)$$

where the subscript MLD indicates values are for MLD variations, and K is a constant.

Although h_k^c and h_k^p can only take on the discrete values of Table 1, h_k^a resulting from the solution of (21) and (2) can take on any value. Thus, it can be thought of as a "floating level" in the analysis system.

With the analysis for h_k^a complete, OTIS sets the temperatures at the gridpoints of Table 1 which are shallower than h_k^a according to

$$(T_k^a)_m = (T_k^a)_0 + \sum_{n=1}^m (\Delta T_k^p)_n \quad (25)$$

where $(T_k^a)_m$ is the analyzed temperature at level m , $(T_k^a)_0$ is the analyzed SST, and $(\Delta T_k^p)_n$ is the change in TOPS predicted temperature from level $n - 1$ to level n (level 0 implies the surface). Thus, the shape of the temperature profile from the surface to the base of the mixed layer (e.g., isothermal, weakly stratified, or multiple thermocline) is controlled exactly by TOPS.

c. Sub-mixed-layer analysis

Following conclusion of the mixed-layer analysis at gridpoint k , OTIS performs an analysis for temperature at and below the analyzed MLD. Below this level, OTIS utilizes a completely variable or "floating" vertical grid designed to concentrate resolution in regions of high vertical gradient. Beginning at the MLD and working downward, the mesh spacing of this floating grid Δz is defined as

$$\Delta z = 50 \text{ m} + (400 \text{ m}^2 \text{ C}^{-1}) \frac{\partial T_k^p}{\partial z} \\ + (10 \text{ m}^3 \text{ C}^{-2}) \frac{\partial^2 T_k^p}{\partial z^2} \quad \text{for } 5 \text{ m} \leq \Delta z \leq 80 \text{ m} \quad (26)$$

with z taken positive downward from the sea surface.

With the vertical grid extending from the base of the mixed layer downward to 400 m defined by (26), OTIS performs an analysis for temperature at each of these levels. This analysis is carried out by solving (1) and (2) at each of the floating levels.

In general, the bathy observations which contribute to the sub-mixed-layer analysis extend to varying depths. Bathys which reach to less than 250 m, or which have $\frac{\partial}{\partial z} |(T_i'' - T_i^c)| > 0.01^\circ \text{C m}^{-1}$ near their deepest reported depth z_B , are used in the analysis only for levels above z_B . Bathys extending to greater than 250 m depth for which

$$\frac{\partial}{\partial z} |(T_i'' - T_i^c)| < 0.01^\circ \text{C m}^{-1}$$

near z_B are used in the analysis at all levels down to 400 m, however, by extrapolating $(T_i'' - T_i^c)$ downward. The mean-square error added to the extrapolated anomaly below z_B by this process is estimated from

$$(\sigma_i'')_{\text{EX}}^2 = \{0.0225 + 0.02 \\ \times \exp[-0.05(z_B - 250)]\}(z - z_B) \quad (27)$$

where z is the depth of the extrapolation point for the i th bathy in meters. Equation (7) for extrapolated bathy observations below z_B then becomes

$$(\sigma_i'')_{\text{BATHY}}^2 = \epsilon_{\text{BATHY}}^2 + (\sigma_i'')^2 + (\sigma_i'')_{\text{EX}}^2 \quad (28)$$

The quantities η_{ij} , λ_i'' , and λ_k'' required in (2) are derived from the user-specified parameters A_k , B_k , C_k , λ_i'' and ϵ_{BATHY} as before. In calculating λ_i'' and λ_k'' via (4), (5), and (7), the quantities σ_i' , σ_i'' and σ_i''' are interpolated linearly from the fixed-levels of Table 1 to the floating levels. Equation (28) is used in place of (7) for extrapolated bathy anomalies below z_B as discussed above. Note that the inverse decorrelation scales A_k , B_k , C_k , and the noise-to-signal ratio λ_i'' for sub-mixed-layer analysis can be assigned values by the user distinctly different from those at the surface. This is particularly important for C_k , which generally has a much smaller value below the MLD reflecting the much longer time scale variability there.

Upon conclusion of the sub-mixed-layer temperature analysis, the analyzed temperature anomalies at the floating levels defined by (26) are vertically interpolated to the fixed levels of Table 1 between the MLD and 400 m depth, added back to climatology, and output.

3. User-specified parameters

The nine user-specified parameters used in OTIS are listed in Table 2. The values of ϵ_{SHIP} and ϵ_{BATHY} are obtained from Earle (1985) and White and Bernstein (1979), respectively. The values of ϵ_{MISST} and ϵ_{MISST} are based on Hawkins et al. (1986) and Strong and McClain (1985). The values of A and B range from $1/(2000 \text{ km})$ in low-latitude open-ocean regions to $1/(200 \text{ km})$ in coastal regions. The values of G and λ'' also vary widely. In general, G is smaller in midlatitude open-ocean regions than in tropical or western bound-

TABLE 2. User-specified parameters.

Parameter	Value
t_{SHIP}	2.29°C
t_{BATHY}	0.20°C
t_{MCSST}	0.71°C
t_{MCSST}	0.22°C
C	1/(20 days) above the MLD, 1/(60 days) below the MLD.
A, B, G, λ^n	Variable, prescribed at the center of $10^\circ \times 20^\circ$ latitude/longitude rectangles and interpolated linearly to gridpoint locations. Separate values for above and below the MLD. A ranges from 1/(200 km) to 1/(2000 km), B ranges from 1/(200 km) to 1/(1000 km), G ranges from 0.1° to 1.0°C, and λ^n ranges from 0.8 to 6.0.

any current regions, where the atmospheric forcing and/or physics of TOPS is not fully adequate. In general, λ^n is smaller in quiescent regions (e.g., eastern Pacific) than in dynamically active regions characterized by strong mesoscale eddies which are unresolved by the horizontal grid (e.g., Kuroshio or Gulf Stream regions).

4. Data selection and screening

Before the analysis begins, thinning and quality-control algorithms are applied to the data. First, the bathy data are screened by applying a sorting process which limits the bathy data density in $2.5^\circ \times 2.5^\circ$ latitude/longitude squares to the 60 most recent reports, with no more than 30 taken from the same platform. This thinning process is a practical necessity for handling ocean weather stations, which typically report two bathy observations per day.

Prior to computing the climatological anomalies from the observations, all data are checked for physically unreasonable temperatures. Any observations reporting less than -2°C or more than 40°C are discarded. Once the observed anomalies are computed and passed to the analysis, they are subjected to a gross error check. Any observations which deviate by more than 7°C from climatology are rejected.

In addition, OTIS applies a ship-tracking algorithm to screen out bathy reports with obvious position errors. These types of errors are fairly common in the real-time bathy dataset and result primarily from coding and radio transmission errors (e.g., latitude and longitude transposed, wrong hemisphere, etc.). Thus, OTIS monitors the successive positions of each ship reporting bathys at any time during the previous 60-day period and flags jumps in position which would require impossibly large ship speeds (bathys deployed from aircraft are not tested in this manner). Bathy observations corresponding to the erroneous position reports are excluded from further processing by OTIS.

For the analysis at each gridpoint, OTIS utilizes only data which fall within certain temporal and spatial windows (see Phoebus 1988). For the SST analysis,

the temporal window extends from the OTIS analysis time back 60 hours. For the MLD and sub-mixed-layer analyses, the window extends back 60 days. The spatial window is defined in terms of the spatial correlation scales $1/A$ and $1/B$. The window is defined as plus or minus one correlation scale in the north-south and east-west directions from the gridpoint. At gridpoints where the east-west correlation scale is larger than the north-south correlation scale, as is often the case, this results in a spatial window that is rectangular in shape, extending farther in the east-west direction than in the north-south direction. Variations of A and B with location will alter the size, shape, and orientation of this window from gridpoint to gridpoint, and at various depths for the same grid location.

The area within the appropriate spatial window is searched and, ideally, all observations within the specified window are collected. In practice, however, the number of observations that can be collected is limited to 700 (a limit which is seldom exceeded). During the data search, the correlation of each observation with the gridpoint η_{ik} is computed from Eq. (3). Once all of the observations are collected, they are sorted by these correlations to select the 15 reports most highly correlated with the gridpoint location for potential use in the analysis. If fewer than 15 observations are found, all are retained, subject to one final quality control procedure.

The (up to) 15 selected reports are screened for spurious data using a horizontal consistency check, or buddy check, patterned after that of DiMego et al. (1985). The particular details of the OTIS buddy check are described by Phoebus (1989). Briefly, the inequality

$$|(T_i^n - T_i^c) - (T_j^n - T_j^c)| \leq (a - b\eta_{ij})\sigma_k^c \quad (29)$$

is examined for each pair of observations. If the inequality is satisfied, observations i and j corroborate each other and are thus both given "keep flags" equal to the correlation between them η_{ij} ; if the inequality is not satisfied, the observations contradict each other and are thus both given "toss flags" equal to η_{ij} . Following examination of all remaining pairs of reports, the single observation with the highest summation of toss flags is removed if the summation exceeds 2. However, observations whose keep flags sum to 2 or more are retained regardless of toss flag settings. This process, beginning with the examination of the inequality (29) and with all flag summations reset to 0, is then repeated until no observations have toss flags which sum to more than 2. The remaining observations are utilized in the analysis at the gridpoint.

Equation (29) states that the absolute temperature difference between two anomalies is compared to some tolerance which is a function of the correlation between them η_{ij} and the long-term rms variation of the thermal anomalies about climatology σ_k^c . Conceptually, observations which are more highly correlated with one another are expected to agree more closely, and temper-

ature differences in regions of high expected rms departures from climatology are given more tolerance. The use of the correlation η_{ij} as the flag value is also a subtle way to control the impact one observation has on the retention or rejection of another. Observations which are highly correlated contribute more to the toss or keep flag summations of one another than do those observations which are farther separated in space and time. Currently, the values of a and b are set to 3.0 and 1.5, respectively. These values were chosen simply through trial and error (see Phoebus 1989).

5. Qualitative comparison of OTIS and TEOTS

a. Surface thermal fields

The OTIS SST field for 28 March 1988 is shown in Fig. 1. This graphic, and the ones to follow, were produced by interpolating the fields (via a Bessel technique) from the standard FNOC NHEM and SHEM 63×63 polar stereographic grids to the standard FNOC 73×144 , 2.5 degree spherical grid, and then contouring.

Though the grid resolution in the model is too coarse to accurately represent fronts, OTIS shows large horizontal SST gradients in the South China Sea, the Sea of Japan, the Kuroshio region and, particularly, in the Gulf Stream region. The tropical western Pacific SST field is quite featureless, while the eastern tropical Pacific shows much structure suggestive of upwelling along the equator and off the coast of Peru.

The OTIS SST field for 28 April 1988 is shown in Fig. 2. Comparison of Figs. 1 and 2 illustrates the expected temporal variability of the large-scale thermal field over one month's time; OTIS shows SST increases

in the upper- and midlatitudes of the Northern Hemisphere associated with the springtime warming. A much more prominent change over this period, however, is the cooling along the equator in the eastern Pacific. Most likely due to enhanced equatorial upwelling in response to stronger than normal easterly winds associated with the "La Niña" weather pattern, this cooling trend led to the coldest June SST anomalies in the eastern tropical Pacific since the early 1970s (Climate Analysis Center 1988).

The OTIS SST anomaly field for 28 March 1988 is shown in Fig. 3. Numerous features are prominent, including: 1) a cold anomaly extending across most of the Pacific between 35° and 45° N, 2) a warm anomaly oriented WSW-ENE in the subtropical western Pacific, 3) a warm anomaly in the eastern North Pacific extending southwestward from Baja California, 4) a cold anomaly along the equator at 125° W, 5) a cold anomaly in the South Pacific centered at 40° S, 110° W, 6) a warm anomaly off the coast of Chile at 30° S, 90° W, and 7) a warm anomaly in the South Atlantic at 20° S, 17° W.

The OTIS SST anomaly field on 28 April 1988 is shown in Fig. 4. Comparison of Figs. 3 and 4 illustrates changes in the OTIS SST anomaly field over one month's time. The midlatitude cold anomaly across most of the Pacific on 28 March extends farther south and shows a larger amplitude on 28 April. The WSW-ENE warm anomaly in the subtropical western Pacific on 28 March is essentially gone by 28 April, replaced by two small warm anomalies centered at 15° N, 132° E and 22° N, 172° W, and a larger warm anomaly centered at 26° N, 160° E. The warm anomaly extending southwestward from Baja California on 28 March ex-

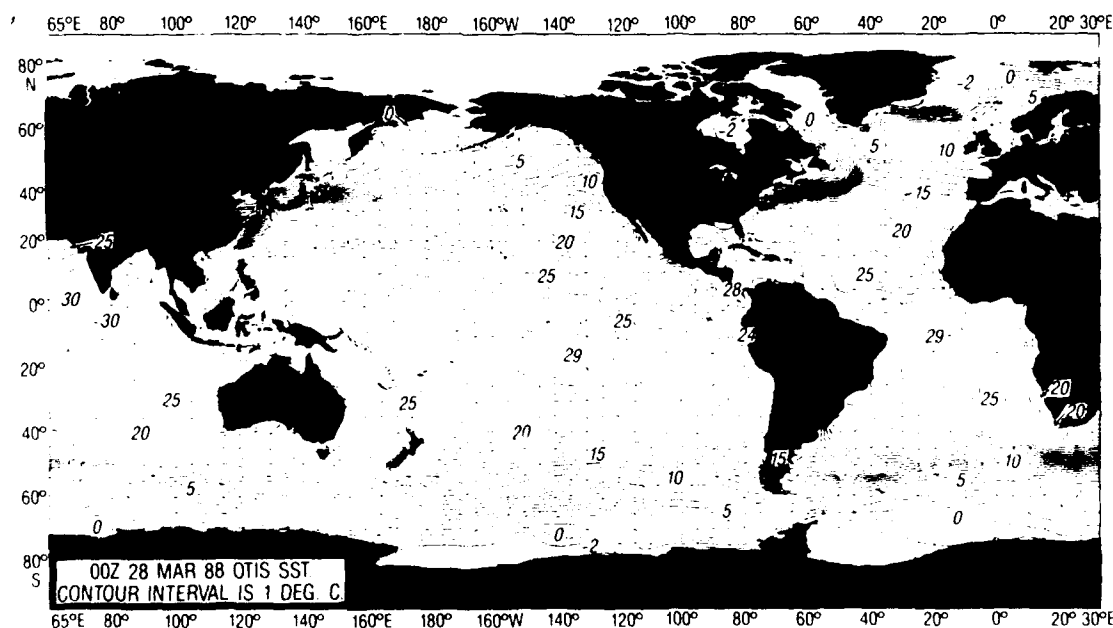


FIG. 1. Sea surface temperature (SST) field from OTIS on 28 March 1988. The contour interval is 1°C .

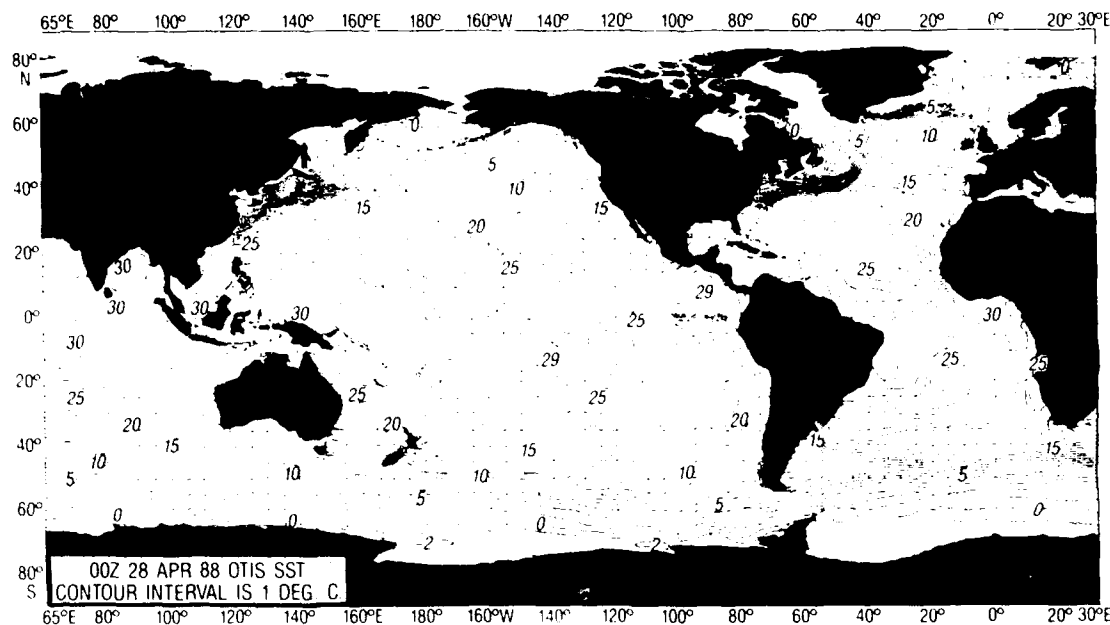


FIG. 2. Sea surface temperature (SST) field from OTIS on 28 April 1988. The contour interval is 1°C.

tends farther north and west by 28 April, and achieves a secondary maximum ENE of Hawaii. The cold anomaly along the equator at 125°W on 28 March moves westward to about 135°W by 28 April, and an even more intense equatorial cold anomaly forms between 85° and 105°W. The cold anomaly at 40°S, 110°W on 28 March weakens and moves northward to 35°S, 120°W by 28 April. The warm anomaly off the coast of Chile at 30°S, 90°W on 28 March re-

mains evident but weakened on 28 April. The warm anomaly in the South Atlantic at 30°S, 17°W on 28 March weakens and moves westward to 30°S, 27°W by 28 April.

The TEOTS SST and SST anomaly fields on 28 March and 28 April (not shown) exhibit very little qualitative difference with the OTIS fields of Figs. 1-4. Thus, though they employ rather different data assimilation techniques (Holl et al. 1979; Clancy and

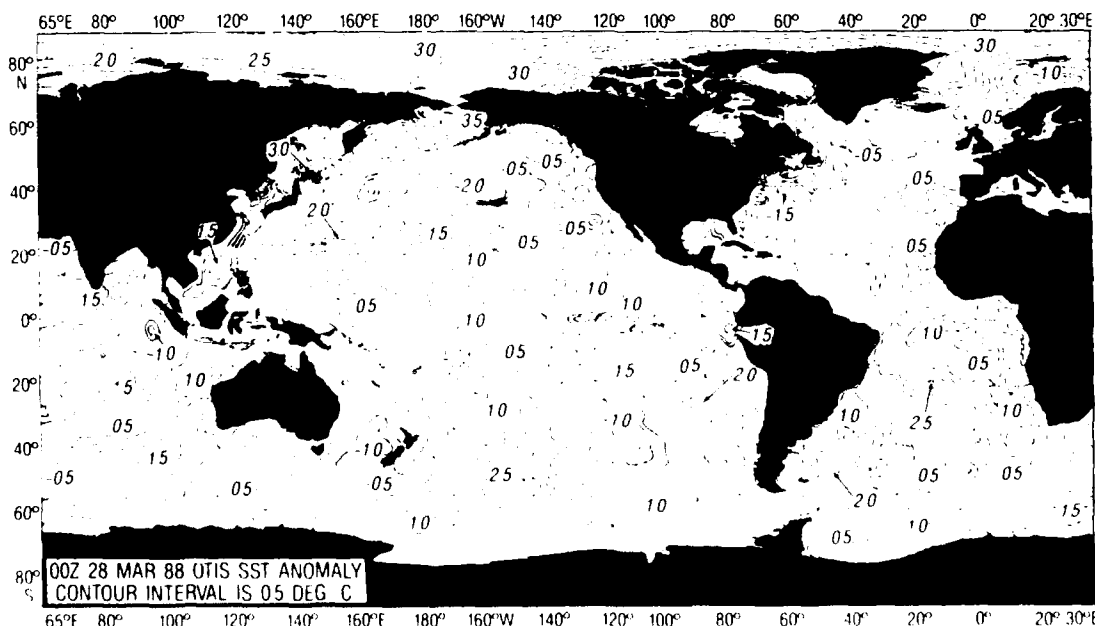


FIG. 3. Sea surface temperature (SST) anomaly field from OTIS on 28 March 1988. The contour interval is 0.5°C. Positive contours are dashed and negative contours are displayed with a thin solid line.

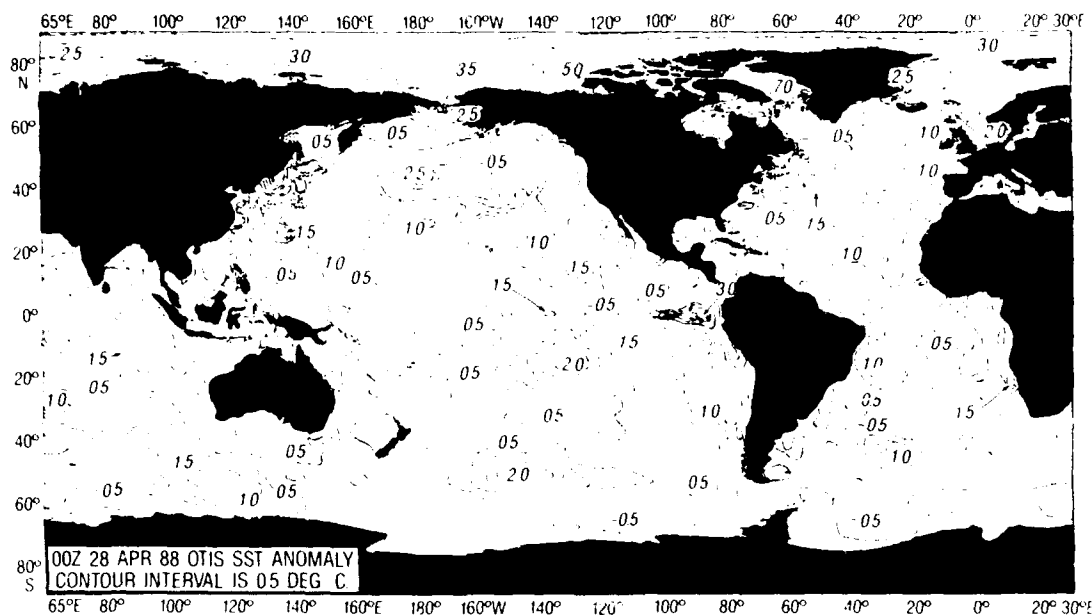


FIG. 4. Sea surface temperature (SST) anomaly field from OTIS on 28 April 1988. The contour interval is 0.5°C. Positive contours are dashed and negative contours are displayed with a thin solid line.

Pollak 1983), the two analysis systems produce very similar SST products on the global scale. This probably reflects the abundance of MCSST data available to them.

Also, the 28 March and 28 April OTIS SST anomaly fields are generally in good agreement with the SST anomaly fields of NOAA (1988a, 1988b, 1988c). Note that a direct quantitative comparison of the OTIS and NOAA SST anomaly fields is beyond the scope of this paper and is not particularly meaningful in any case

since the NOAA product represents a monthly averaged field while the OTIS product represents a daily-averaged field.

b. Subsurface thermal fields

The OTIS and TEOTS temperature at 200 m depth (T_{200}) fields for 28 March 1988 are shown in Fig. 5. In general, OTIS produces sharper horizontal gradients in the T_{200} thermal field, particularly in the subtropical

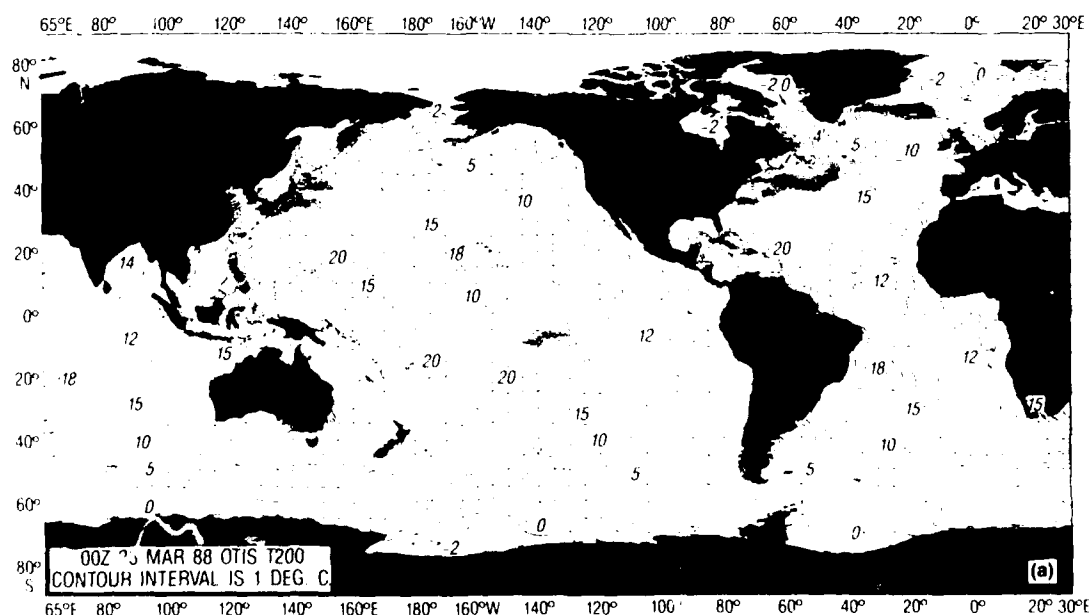


FIG. 5a. Temperature at 200 m depth (T_{200}) from OTIS on 28 March 1988. The contour interval is 1°C.

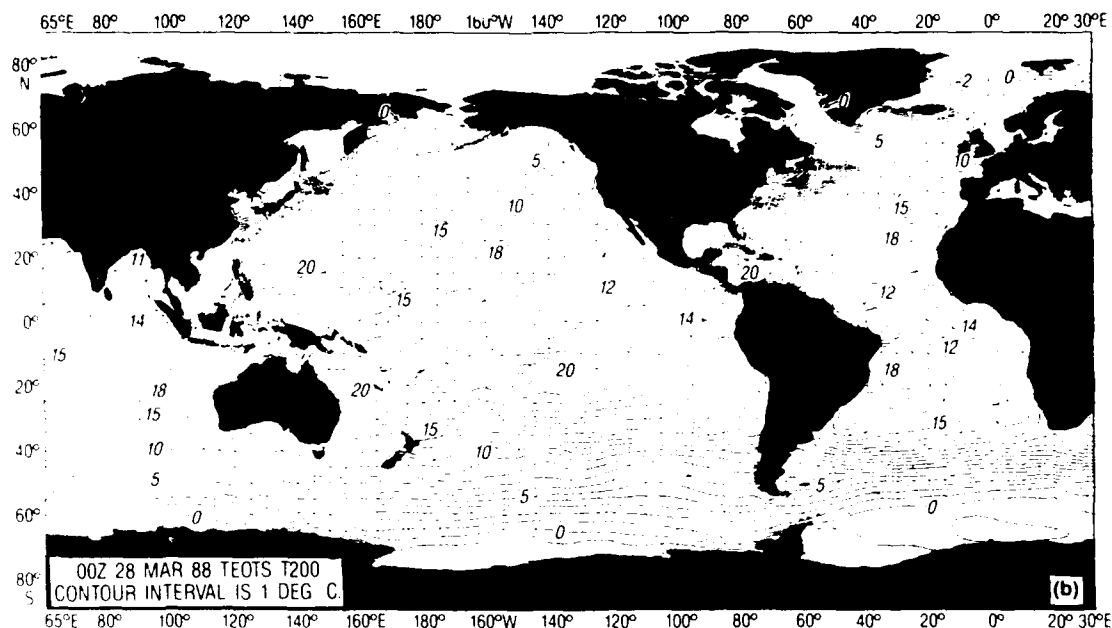


FIG. 5b. As in Fig. 5a, but for TEOTS.

Pacific and Atlantic. OTIS provides a better representation of the western boundary currents at 200 m depth than TEOTS, including 1) separation of the high gradient zones of the Kuroshio and the Oyashio, 2) a more physically realistic orientation and packing of the isotherms in the Kuroshio south of Japan, 3) tighter packing of isotherms in the Gulf Stream extension region between 60° and 35°W, and 4) a more physically realistic orientation and packing of isotherms west of 70°W and south of Cape Hatteras. In addition, the

OTIS T200 field shows a clear (though poorly resolved) representation of the Loop Current in the Gulf of Mexico. This feature is all but absent in the TEOTS T200 field.

The OTIS and TEOTS temperature anomaly fields at 200 m depth (T200 anomaly) for 28 March 1988 are shown in Fig. 6. Substantial differences are apparent in the T200 anomaly fields produced by the two models. In general, the TEOTS T200 anomaly field appears noisier than the corresponding OTIS field, particularly

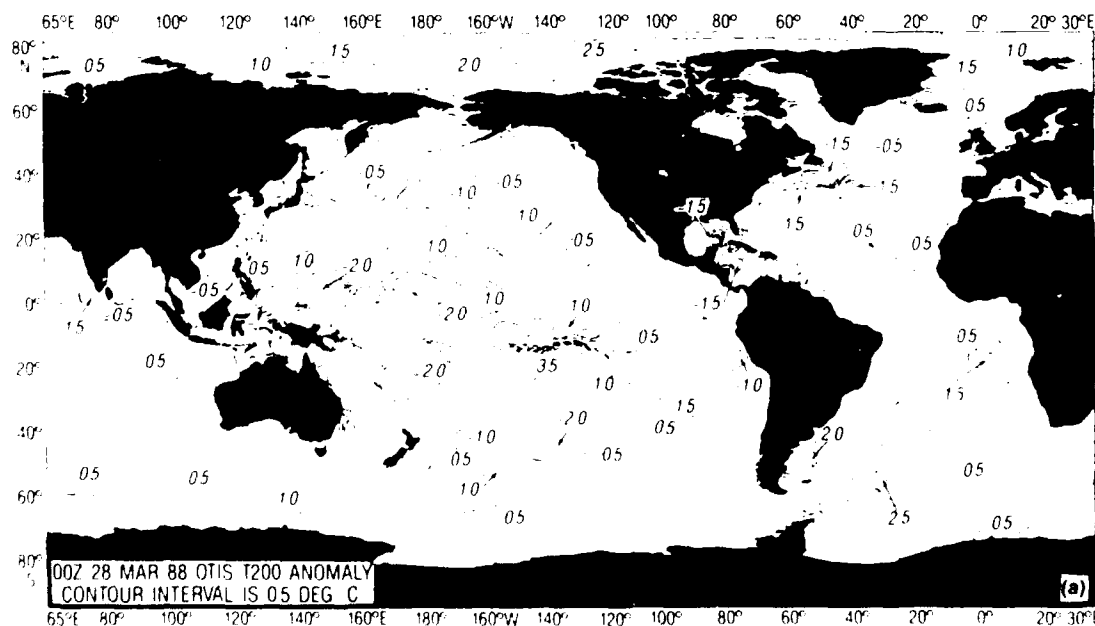


FIG. 6a. Temperature anomaly at 200 m depth (T200 anomaly) from OTIS on 28 March 1988. The contour interval is 0.5°C. Positive contours are dashed and negative contours are displayed with a thin solid line.

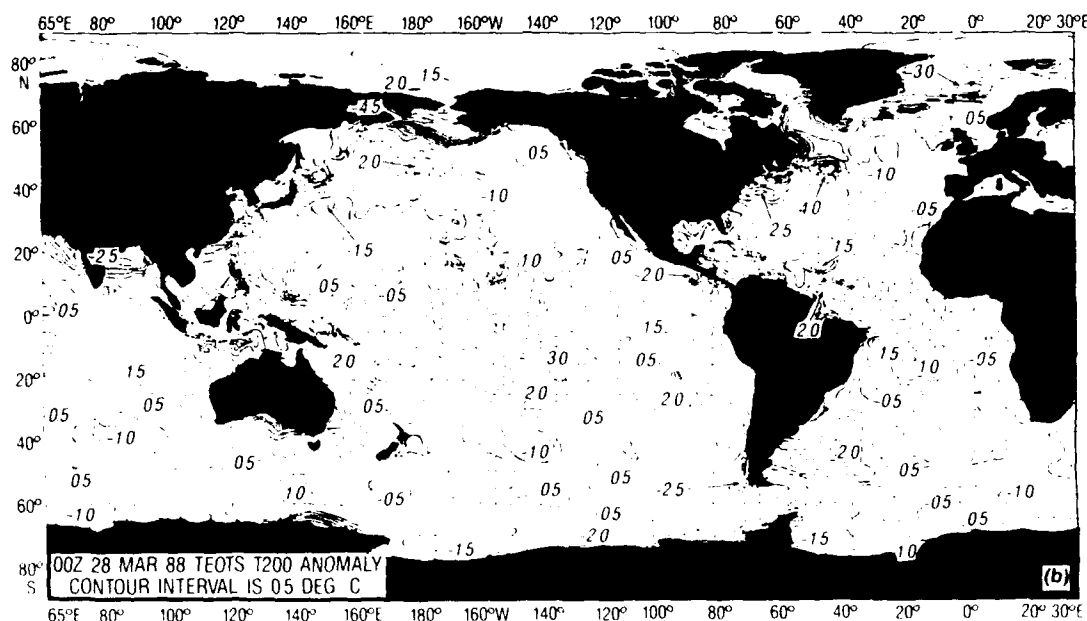


FIG. 6b. As in Fig. 6a, but for TEOTS.

in the tropical Pacific. The features in the OTIS anomaly field generally show more spatial continuity and exhibit a more physically reasonable east-west (vice north-south or circular) pattern. A large warm anomaly extending across most of the tropical South Pacific between 5° and 25° S is present in both the OTIS and TEOTS fields, but the northern and southern boundaries of this anomaly are represented much more sharply by OTIS. This corresponds to the sharper horizontal gradients in the OTIS T200 field for this region which were obvious in Fig. 5.

In some regions, the differences between the OTIS and TEOTS T200 anomalies are quite large. For example, TEOTS shows a warm anomaly of over 2.0°C at 47°N , 177°W , but this feature is not present in the OTIS anomaly field. An even more striking case is the TEOTS warm anomaly of over 4.0°C off the coast of Newfoundland at 45°N , 45°W ; OTIS shows a *cold* anomaly with amplitude greater than 1.5°C in this region.

The large differences between the OTIS and TEOTS T200 anomaly fields are a result of the fact that EOTS/TEOTS performs a vertical blending process from the surface to 400 m depth (Holl et al. 1979; Clancy and Pollak 1983). In the absence of adequate bathy density, this tends to tie subsurface anomalies (even below the mixed layer) to the SST anomaly. Thus, it is never apparent whether subsurface anomalies in EOTS/TEOTS are supported by bathy data, or are the result of this vertical blending process. Also, in the absence of adequate bathy coverage, EOTS/TEOTS can produce a subsurface thermal field which is *worse* than climatology if the real thermal anomaly changes sign with depth. For example, if there is sufficient surface data to map a warm anomaly at the surface, but in-

sufficient bathy data to map the field at 200 m depth, then the EOTS vertical blending will tend to force in a warm anomaly at 200 m. But, if there is actually a *cold* anomaly at 200 m, then the EOTS/TEOTS temperature at this depth will differ from reality by even more than climatology (i.e., it will be warmer than climatology while reality is colder than climatology). OTIS, on the other hand, performs its equivalent of the EOTS/TEOTS vertical blending process only from the surface down to the base of the mixed layer. Thus, temperature anomalies below the mixed layer in OTIS can arise *only* if the bathy data support them.

The OTIS and TEOTS T200 anomaly fields for 28 April 1988 are shown in Fig. 7. As was the case for 28 March, substantial differences between the OTIS and TEOTS anomalies are evident. OTIS shows warm anomalies in the western North Atlantic, roughly along the path of the Gulf Stream, while TEOTS shows cold anomalies in this region. TEOTS shows warm anomalies in the Indian Ocean (15°S , 90°E), the eastern tropical Pacific (5°S – 20°N , 90° – 140°W), and the western tropical Atlantic (20°S – 15°N , 20° – 60°W) which are not present in the OTIS field.

Comparison of Figs. 6a and 7a illustrate changes in the OTIS T200 anomaly field on a one-month time scale. Most of the features prominent on 28 March are still evident on 28 April. An exception is the cold anomaly at 40°S , 140°W on 28 March; this feature weakens substantially by 28 April. Also, the 1.5 degree warm anomaly southwest of Hawaii (17°N , 165°W) on 28 March increases to a 3.0 degree anomaly by 28 April. Finally, a warm anomaly of more than 2 degrees forms in the western tropical Pacific at 4°N , 136°E between 28 March and 28 April.

The OTIS and TEOTS temperature anomaly fields

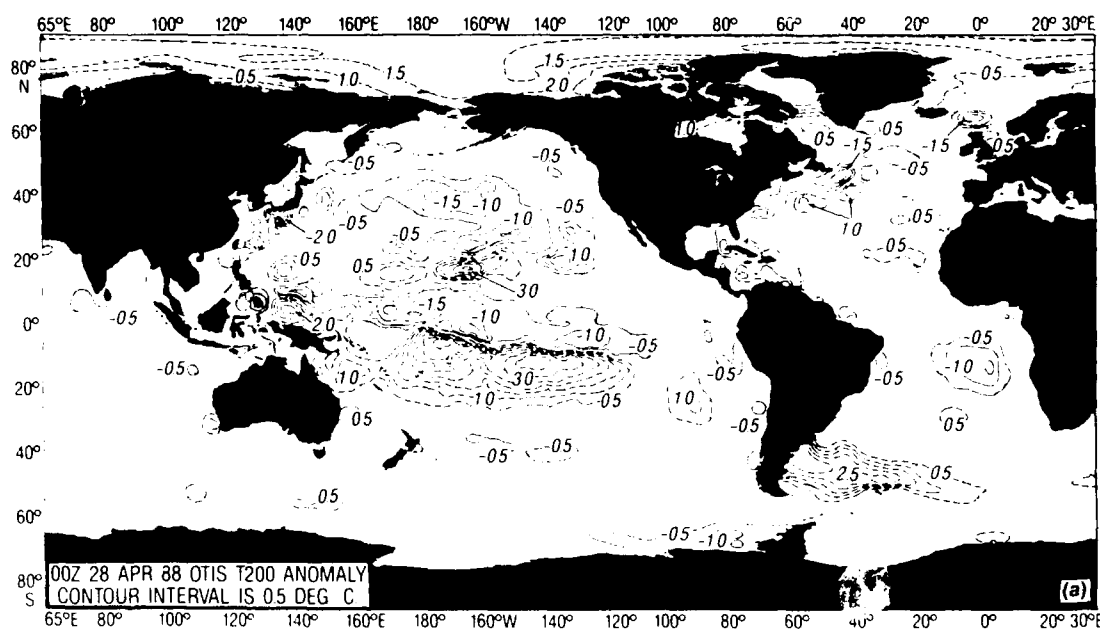


FIG. 7a. Temperature anomaly at 200 m depth (T200 anomaly) from OTIS on 28 April 1988. The contour interval is 0.5°C. Positive contours are dashed and negative contours are displayed with a thin solid line.

at 400 m depth (T400 anomaly) for 28 April 1988 are shown in Fig. 8. Large differences in these fields, which are also a result of the TEOTS vertical blending discussed above, are apparent. For example, in response to and consistent with the bathy data at 400 m depth, OTIS shows a cold anomaly in the central South Pacific between 10 and 20°S. In primary response to its own vertical blending process and without the support of bathy data at 400 m depth, however, TEOTS shows a

warm anomaly in this region and throughout most of the subtropical South Pacific.

6. Quantitative verification of OTIS and TEOTS

a. Procedure

Verification statistics for OTIS and TEOTS were compiled from comparison against independent bathy data. Although the bathy data are subject to errors

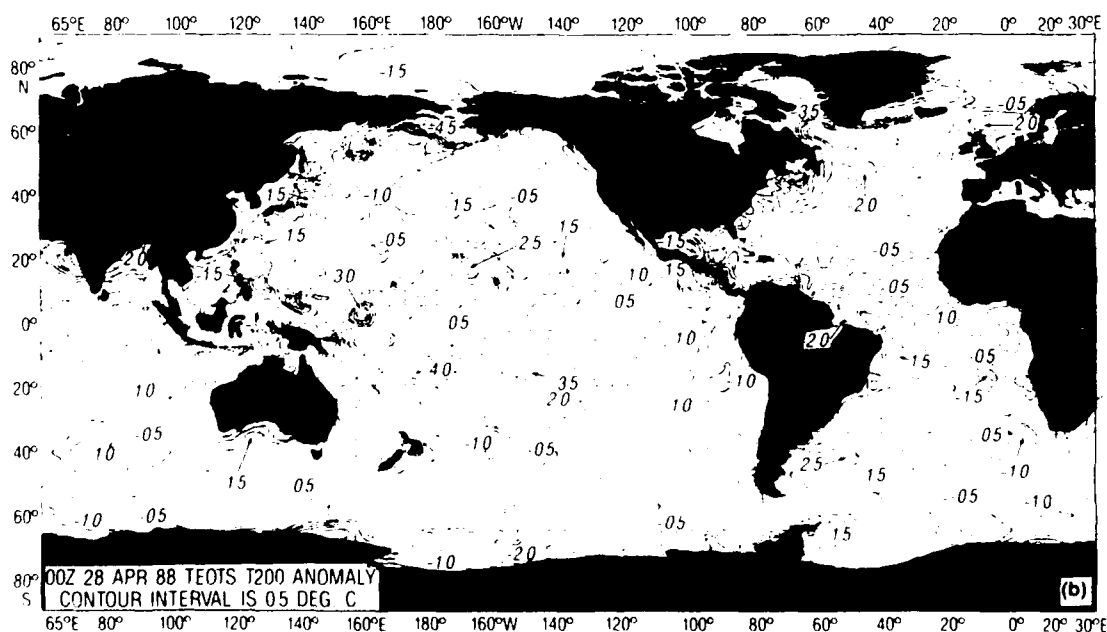


FIG. 7b. As in Fig. 7a, but for TEOTS.

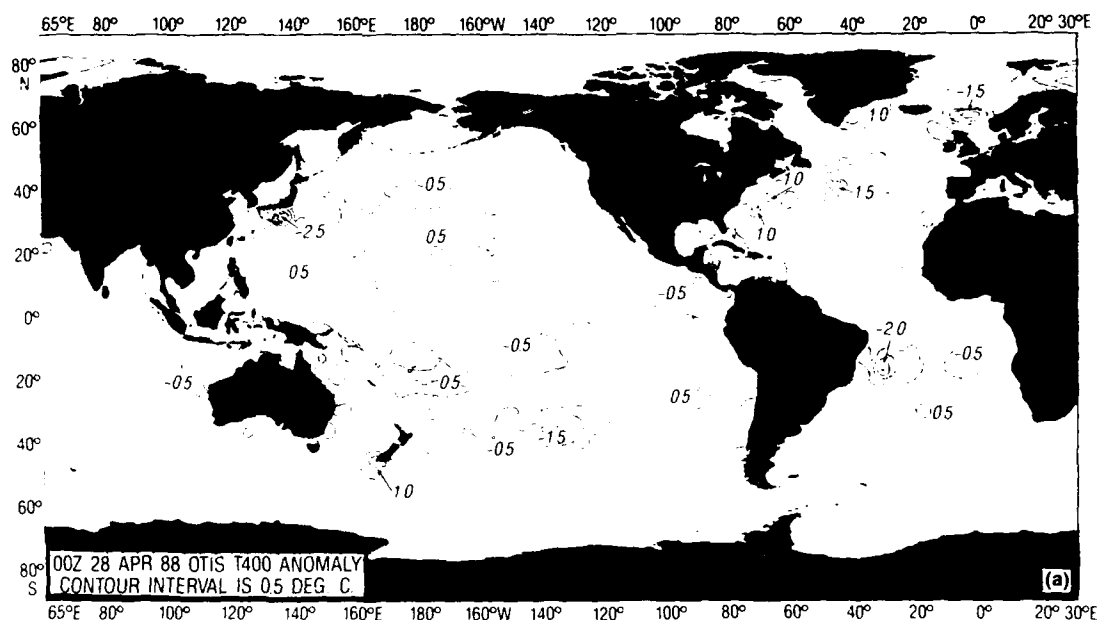


FIG. 8a. Temperature anomaly at 400 m depth (T400 anomaly) from OTIS on 28 April 1988. The contour interval is 0.5°C. Positive contours are dashed and negative contours are displayed with a thin solid line.

which can be quite large (including, in the context of model comparison, errors produced by subgrid-scale features unresolved by the model grids), they still provide an important ground truth reference for ranking the skill of ocean thermal models.

Once per day the thermal fields from OTIS and TEOTS are interpolated via a Bessel technique to the locations of all bathy observations received at FNOG during the previous 24 hours but not yet assimilated

into the models (making the observations independent of the models). Each bathy observation is then vertically interpolated linearly to a standard vertical grid between the surface and 300 m, and spurious observations are discarded automatically by a bathy error detection algorithm, which is less sophisticated than the OTIS quality control procedures discussed in section 4.

The remaining data are used to calculate analyzed

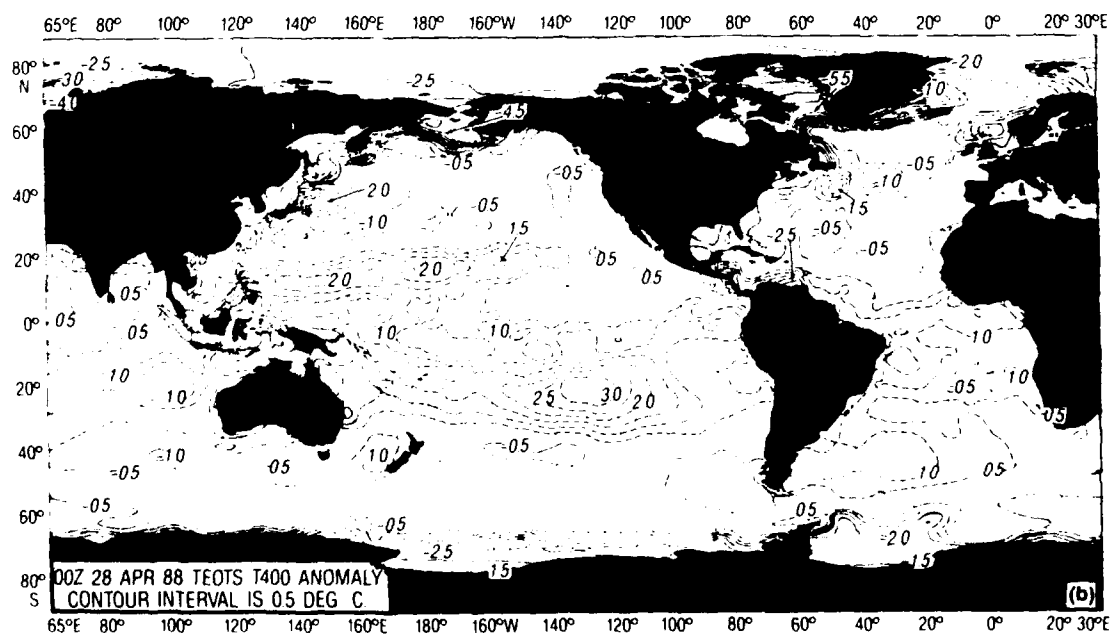


FIG. 8b. As in Fig. 8a, but for TEOTS.

minus observed temperatures (i.e., the "apparent errors" in the analyzed temperatures) for both OTIS and TEOTS at the standard grid depths of 0, 12.5, 25, 50, 75, 100, 150, 200, and 300 m at each bathy location. The resulting apparent errors for both OTIS and TEOTS from each individual bathy at each standard depth are accumulated in a running 90-day history file and segregated into the nine verification areas shown in Fig. 9. From the data in this history file, the apparent root-mean-square (rms) errors for both OTIS and TEOTS are calculated at the standard depths in each of the nine verification areas from the 90-day accumulation of data covering the months of February, March, and April 1988. The total number of data collected and used in these calculations amounts to 9980 bathy observations.

b. Vertical profiles of apparent error

Plots of vertical profiles of the apparent rms errors for OTIS and TEOTS for February–April 1988 for each of the nine verification areas are shown in Figs. 10a–i. The shapes of the error profiles for OTIS and TEOTS in each area are quite similar. All areas except the midlatitude Atlantic areas (Areas 3 and 4, Figs. 10c and 10d) exhibit local maxima in the error profiles at some intermediate depth for both OTIS and TEOTS. These local maxima are quite pronounced for the Indian Ocean (Area 5, Fig. 10e), the tropical eastern Pacific (Area 1A, Fig. 10f), and the tropical eastern Atlantic (Area 3A, Fig. 10h), and are probably due primarily to noise in the verification data caused by unresolved vertical displacements of the strong thermoclines in these areas produced by eddies and internal waves. The midlatitude eastern Atlantic (Area 3, Fig. 10c) is characterized by local minima in the error profiles for both

OTIS and TEOTS at about 100 m depth. The midlatitude western Atlantic (Area 4, Fig. 10d) shows a monotonic decrease in the apparent rms error with depth for OTIS.

Note the large apparent rms errors for OTIS between 25 and 75 m depth in the midlatitude eastern Pacific compared to TEOTS (Area 1, Fig. 10a). From examination of the apparent *mean* errors for this area derived from the same bathy dataset (not shown), it is apparent that the OTIS thermal fields were biased cold in this depth range. This implies that the OTIS MLD was biased shallow in the region, suggesting room for improvement in the TOPS mixed-layer model and/or the manner in which OTIS analyzes MLD.

Except in the midlatitude western Atlantic and the Indian Ocean, where the apparent errors for OTIS indicate the largest relative improvement over TEOTS, the verification statistics show very little difference between the accuracy of the two products at the surface. Improvements of OTIS over TEOTS are most pronounced below about 100–150 m depth. This is consistent with the conclusion of section 2 that the OTIS and TEOTS SST fields are quite similar, while the T200 and T400 fields exhibit substantial differences.

c. Depth-averaged apparent error statistics

Depth-averaged apparent rms error statistics, calculated by integrating the rms errors of Fig. 10 over various depth intervals and then dividing the result by the depth interval, provide a convenient representation of the verification results. Depth-averaged statistics for February–April 1988 are presented in Table 3 for each of the nine verification areas. Included in the tables are depth-averaged apparent rms errors for OTIS and TEOTS and the percent improvement of the depth-

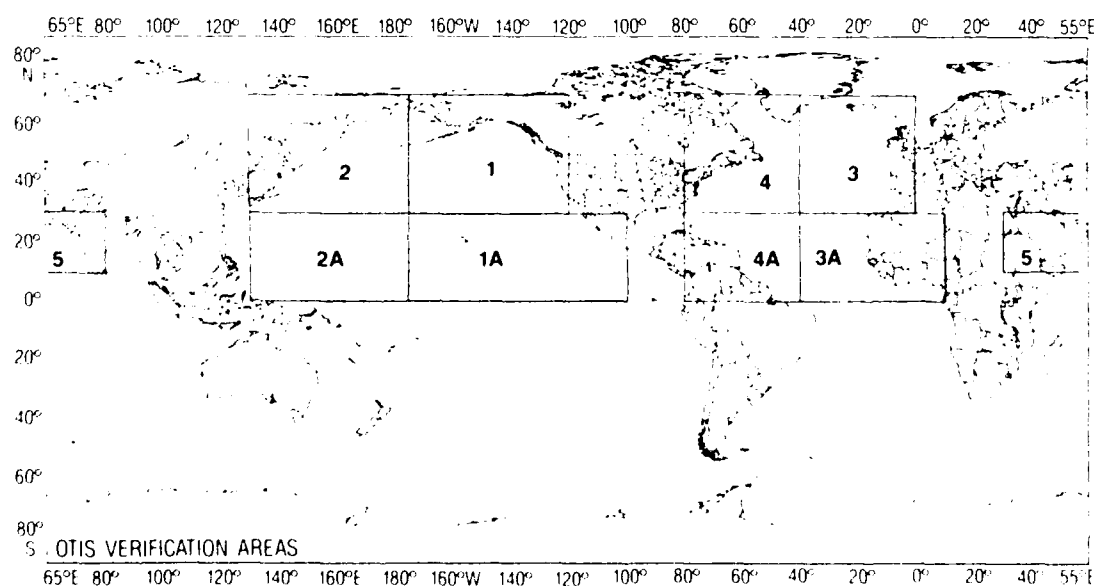


FIG. 9. The nine verification areas in which root-mean-square (rms) errors were calculated for OTIS and TEOTS.

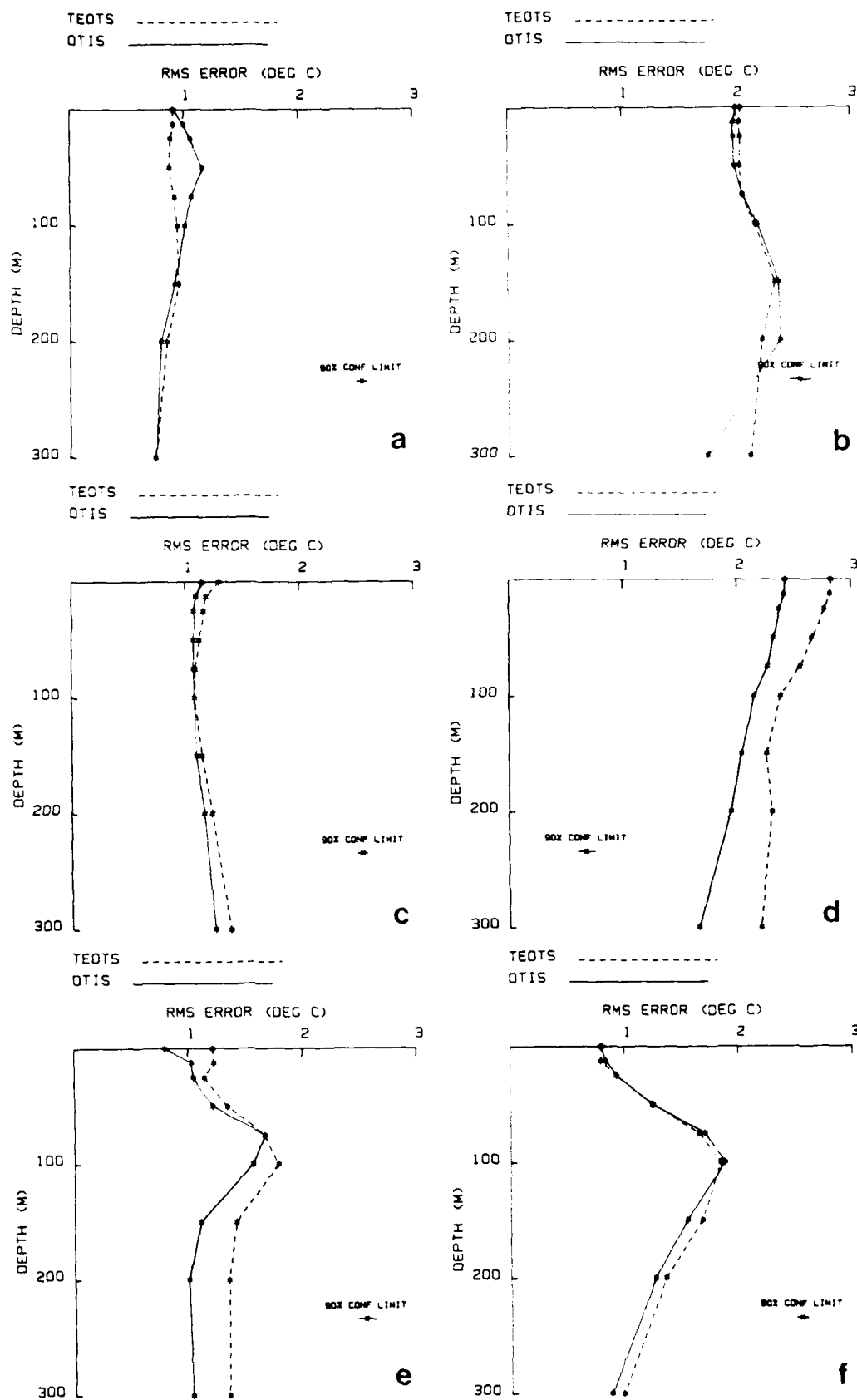


FIG. 10. Apparent root-mean-square (rms) errors for OTIS (solid line) and TEOTS (dashed line) as a function of depth made in February–April 1988. The error bar indicates an approximate 90% confidence interval. (a) In the midlatitude eastern Pacific (Area 1) from 970 independent bathy reports. (b) for the midlatitude western Pacific (Area 2) and 1232 bathys. (c) for the midlatitude eastern Atlantic (Area 3) and 2304 bathys. (d) for the midlatitude western Atlantic (Area 4) and 2161 bathys. (e) for the Indian Ocean (Area 5) and 372 bathys. (f) for the tropical eastern Pacific (Area 1A) and 1295 bathys. (g) for the tropical western Pacific (Area 2A) and 594 bathys. (h) for the tropical eastern Atlantic (Area 3A) and 104 bathys, and (i) for the tropical western Atlantic (Area 4A) and 948 bathys.

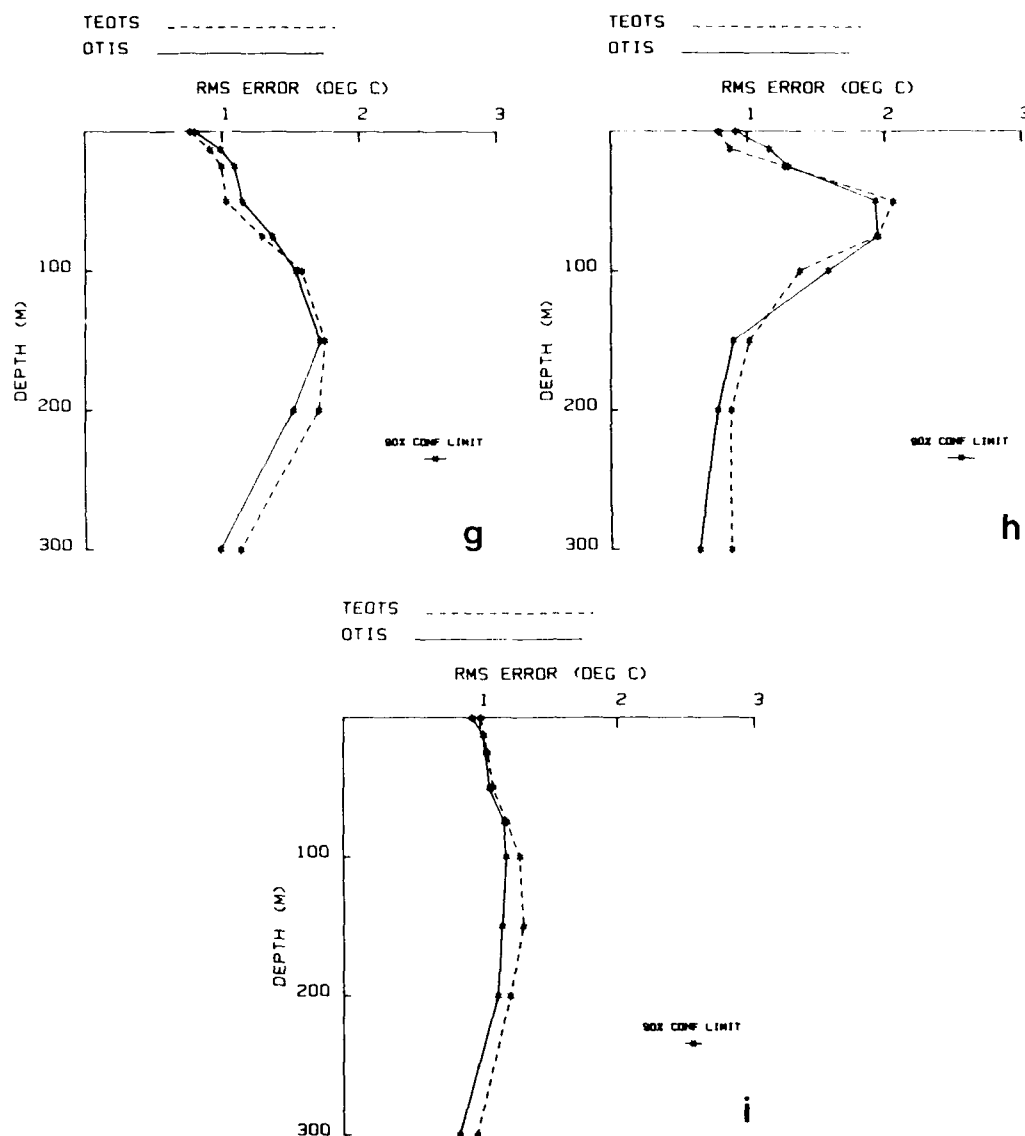


FIG. 10. (Continued)

averaged OTIS rms error over that of TEOTS for depth intervals of 0–300 m, 0–150 m, and 150–300 m.

The statistics in Table 3 show regional differences, with the apparent rms errors for both OTIS and TEOTS largest in the midlatitude western Atlantic (Area 4) and midlatitude western Pacific (Area 2). This reflects the influence of the Gulf Stream and Kuroshio Current systems and their related mesoscale eddy fields. The relative improvement of OTIS over TEOTS is largest in the Indian Ocean (Area 5). OTIS performs poorest relative to TEOTS in the midlatitude eastern Pacific (Area 1) because of its shallow bias in MLD noted above, but *both* OTIS and TEOTS are extremely accurate there with low apparent rms errors relative to the other areas and climatology. When averaged over

all areas (9980 bathy reports), OTIS shows a 7% improvement over TEOTS in 0–300 m apparent rms error. Stratified by depth ranges, OTIS shows only a 3% improvement over TEOTS in 0–150 m apparent rms error, but an 11% improvement over TEOTS in 150–300 m apparent rms error.

It is useful to compare the accuracy of OTIS to that of the ocean thermal climatology used as the first-guess field. Depth-averaged apparent rms errors for OTIS and this climatology for February–April in the nine verification areas are shown in Table 4. Also included in the table is the percent improvement of OTIS over the climatology. Averaged over all areas, OTIS shows a 12% improvement over climatology in 0–300 m apparent rms error. The improvement relative to cli-

TABLE 3. Depth-averaged apparent rms error statistics, $[(\sigma^a)^2]^{0.5}$, for OTIS and TEOTS for February–April 1988.

Area	Area definition	Number of obs	OTIS rms error (C)	TEOTS rms error (C)	Percent improvement of OTIS over TEOTS
<i>Depth interval = 0–300 m</i>					
1	Midlatitude EPAC	970	0.92	0.88	4
2	Midlatitude WPAC	1232	2.14	2.17	1
3	Midlatitude ELANT	2304	1.14	1.20	5
4	Midlatitude WLANT	2161	2.06	2.40	14
5	Indian Ocean	372	1.17	1.42	18
1A	Tropical EPAC	1295	1.31	1.37	4
2A	Tropical WPAC	594	1.35	1.41	4
3A	Tropical ELANT	104	1.12	1.17	4
4A	Tropical WLANT	948	1.08	1.17	8
Average over all areas			1.36	1.46	7
<i>Depth interval = 0–150 m</i>					
1	Midlatitude EPAC	970	1.03	0.92	12
2	Midlatitude WPAC	1232	2.11	2.12	1
3	Midlatitude ELANT	2304	1.08	1.13	4
4	Midlatitude WLANT	2161	2.24	2.54	12
5	Indian Ocean	372	1.31	1.48	12
1A	Tropical EPAC	1295	1.44	1.44	0
2A	Tropical WPAC	594	1.34	1.30	3
3A	Tropical ELANT	104	1.49	1.44	3
4A	Tropical WLANT	948	1.12	1.18	6
Average over all areas			1.46	1.51	3
<i>Depth interval = 150–300 m</i>					
1	Midlatitude EPAC	970	0.80	0.83	4
2	Midlatitude WPAC	1232	2.17	2.21	2
3	Midlatitude ELANT	2304	1.19	1.27	7
4	Midlatitude WLANT	2161	1.87	2.26	18
5	Indian Ocean	372	1.03	1.36	24
1A	Tropical EPAC	1295	1.19	1.29	8
2A	Tropical WPAC	594	1.37	1.52	10
3A	Tropical ELANT	104	0.75	0.90	16
4A	Tropical WLANT	948	1.04	1.15	10
Average over all areas			1.27	1.42	11

matology is largest in the midlatitude eastern Pacific (Area 1), and smallest in the tropical western Atlantic (Area 4A).

d. Depth-averaged grid-scale error statistics

It may seem surprising that the differences in apparent rms error between OTIS, TEOTS, and climatology are not larger, given the qualitative differences between the subsurface thermal fields noted in section 5. To explain this, we write expressions for the apparent rms errors $[(\sigma^a)^2]^{0.5}$ for OTIS, TEOTS, and climatology as

$$[(\sigma^a)_{\text{OTIS}}^2]^{0.5} = [(\sigma^a)_{\text{OTIS}}^2 + (\sigma^n)^2 + \epsilon_{\text{BATHY}}^2]^{0.5} \quad (30)$$

$$[(\sigma^a)_{\text{TEOTS}}^2]^{0.5} = [(\sigma^a)_{\text{TEOTS}}^2 + (\sigma^n)^2 + \epsilon_{\text{BATHY}}^2]^{0.5} \quad (31)$$

$$[(\sigma^a)_{\text{CLIM}}^2]^{0.5} = [(\sigma^a)_{\text{CLIM}}^2 + (\sigma^n)^2 + \epsilon_{\text{BATHY}}^2]^{0.5} \quad (32)$$

where the overbar indicates an average over all bathy data in a verification area, and the grid-scale error σ^a , the subgrid-scale error σ^n , and the bathy instrumental error ϵ_{BATHY} are assumed to be uncorrelated. With the thermal fields produced by the two models and climatology all defined on the same horizontal grid, differences in apparent rms error $[(\sigma^a)^2]^{0.5}$ can be due only to differences in σ^a . However, for the grid resolution used here (about 320 km), $\sigma^a \approx \sigma^n \gg \epsilon_{\text{BATHY}}$. Thus, the apparent rms error statistics are highly contaminated by subgrid-scale noise (σ^n) which tends to overwhelm and mask the true grid-scale error of the fields (σ^a) and, hence, the differences in the relative performance of the models.

TABLE 4. Depth-averaged apparent rms error statistics, $[(\sigma')^2]^{0.5}$, for OTIS and climatology for February–April 1988.

Area	Area definition	Number of obs	OTIS rms error (°C)	CLIM rms error (°C)	Percent improvement of OTIS over CLIM
<i>Depth interval 0–300 m</i>					
1	Midlatitude EPAC	970	0.92	1.24	26
2	Midlatitude WPAC	1232	2.14	2.23	4
3	Midlatitude ELANT	2304	1.14	1.21	6
4	Midlatitude WLANT	2161	2.06	2.57	20
5	Indian Ocean	372	1.17	1.22	4
1A	Tropical EPAC	1295	1.31	1.57	17
2A	Tropical WPAC	594	1.35	1.60	16
3A	Tropical ELANT	104	1.12	1.21	7
4A	Tropical WLANT	948	1.08	1.09	1
Average over all areas			1.36	1.55	12
<i>Depth interval 0–150 m</i>					
1	Midlatitude EPAC	970	1.03	1.38	26
2	Midlatitude WPAC	1232	2.11	2.14	1
3	Midlatitude ELANT	2304	1.08	1.15	5
4	Midlatitude WLANT	2161	2.24	2.65	16
5	Indian Ocean	372	1.31	1.28	2
1A	Tropical EPAC	1295	1.44	1.62	11
2A	Tropical WPAC	594	1.34	1.41	5
3A	Tropical ELANT	104	1.49	1.49	0
4A	Tropical WLANT	948	1.12	1.04	7
Average over all areas			1.46	1.57	7
<i>Depth interval 150–300 m</i>					
1	Midlatitude EPAC	970	0.80	1.10	27
2	Midlatitude WPAC	1232	2.17	2.32	6
3	Midlatitude ELANT	2304	1.19	1.27	7
4	Midlatitude WLANT	2161	1.87	2.49	25
5	Indian Ocean	372	1.03	1.15	11
1A	Tropical EPAC	1295	1.19	1.53	22
2A	Tropical WPAC	594	1.37	1.79	24
3A	Tropical ELANT	104	0.75	0.94	20
4A	Tropical WLANT	948	1.04	1.14	9
Average over all areas			1.27	1.53	17

Contamination of ocean thermal verification statistics with observational noise is a fairly general problem, even for finer-resolution models. A technique for estimating the uncontaminated grid-scale errors of a model would be quite useful, and can be derived from the formalism presented above. From (30)–(32),

$$[(\sigma')^2_{\text{OTIS}}]^{0.5} = [(\sigma')^2_{\text{CLIM}} + (\sigma')^2_{\text{OTIS}} - (\sigma')^2_{\text{CLIM}}]^{0.5} \quad (33)$$

$$[(\sigma')^2_{\text{TEOTS}}]^{0.5} = [(\sigma')^2_{\text{CLIM}} + (\sigma')^2_{\text{TEOTS}} - (\sigma')^2_{\text{CLIM}}]^{0.5} \quad (34)$$

The quantity $(\sigma')^2_{\text{CLIM}}$ is the mean-square departure of the thermal field from climatology (i.e., the mean-square of the anomaly field) calculated over the locations of the bathy observations in each verification area. It can be estimated from the analyzed anomalies during

the study period. Thus, all of the terms on the right-hand-side of (33) and (34) can be obtained to yield estimates of the grid-scale rms errors of the models ($[(\sigma')^2_{\text{OTIS}}]^{0.5}$ and $[(\sigma')^2_{\text{TEOTS}}]^{0.5}$) uncontaminated by observational noise.

Depth-averaged values of the grid-scale rms errors $[(\sigma')^2]^{0.5}$ for OTIS and TEOTS calculated from (33) and (34) are presented in Table 5. For all depth intervals and areas, the grid-scale rms errors of Table 5 are smaller than the apparent rms errors of Table 3, reflecting the removal of observational noise. Also, the grid-scale errors do not as clearly take on relative maxima in the western boundary current areas (Areas 2 and 4) as the apparent errors. This again reflects the suppression of observational noise, which is particularly strong in these areas due to the presence of strong and unresolved mesoscale eddies. Comparison of the grid-scale errors rather than the apparent errors allows a

TABLE 5. Depth-averaged grid-scale rms error statistics, $[(\sigma^2)^{1/2}]^\circ$, for OTIS and TEOTS for February–April 1988.

Area	Area definition	Number of obs	OTIS rms error ($^\circ$)	TEOTS rms error ($^\circ$)	Percent improvement of OTIS over TEOTS
<i>Depth interval 0–300 m</i>					
1	Midlatitude EPAC	970	0.55	0.48	14
2	Midlatitude WPAC	1232	1.00	1.06	6
3	Midlatitude EI ANI	2304	0.58	0.69	16
4	Midlatitude WL ANI	2161	0.73	1.43	49
5	Indian Ocean	372	0.69	1.06	35
1A	Tropical EPAC	1295	0.81	0.90	10
2A	Tropical WPAC	594	0.96	1.06	10
3A	Tropical EI ANI	104	0.62	0.71	13
4A	Tropical WL ANI	948	0.53	0.69	23
Average over all areas			0.72	0.90	20
<i>Depth interval 0–150 m</i>					
1	Midlatitude EPAC	970	0.61	0.39	56
2	Midlatitude WPAC	1232	1.12	1.15	3
3	Midlatitude EI ANI	2304	0.20	0.36	44
4	Midlatitude WL ANI	2161	0.93	1.49	38
5	Indian Ocean	372	0.87	1.11	22
1A	Tropical EPAC	1295	0.92	0.92	0
2A	Tropical WPAC	594	1.02	0.98	4
3A	Tropical EI ANI	104	0.83	0.75	11
4A	Tropical WL ANI	948	0.62	0.73	15
Average over all areas			0.79	0.88	10
<i>Depth interval 150–300 m</i>					
1	Midlatitude EPAC	970	0.48	0.53	10
2	Midlatitude WPAC	1232	0.85	0.95	11
3	Midlatitude EI ANI	2304	0.89	1.00	11
4	Midlatitude WL ANI	2161	0.44	1.35	68
5	Indian Ocean	372	0.48	1.01	53
1A	Tropical EPAC	1295	0.68	0.85	20
2A	Tropical WPAC	594	0.93	1.14	18
3A	Tropical EI ANI	104	0.45	0.66	32
4A	Tropical WL ANI	948	0.43	0.66	35
Average over all areas			0.62	0.90	31

more meaningful ranking of model skill. The 0–300 m grid-scale rms errors of Table 5 averaged over all areas show OTIS with a 20% improvement over TEOTS, three times that calculated from the apparent rms error statistics of Table 3.

7. Summary, conclusions, and future work

OTIS is an ocean thermal analysis system designed for operational use at FNOG. It is based on the optimum interpolation data assimilation technique and functions in an analysis–prediction–analysis data assimilation cycle with the TOPS mixed-layer model. OTIS provides a rigorous framework for combining real-time data (e.g., ship, buoy, bathy, and satellite observations), climatology, and predictions from numerical ocean prediction models (e.g., TOPS) to produce a large-scale synoptic representation of ocean thermal structure.

An operational test of OTIS was conducted during February, March, and April of 1988. This involved running OTIS daily in parallel with and on the same grid as the TEOTS analysis (the existing operational product), comparing output from the two models qualitatively, and validating the output of the models against bathy data that was independent of the models.

Qualitative comparison of SST fields produced by OTIS and TEOTS shows little difference between the two products. Comparison of subsurface fields, however, shows large and important differences between the two. OTIS subsurface temperature fields exhibit sharper and more realistic horizontal gradients, more physically reasonable large-scale anomaly patterns, a better (though still very poorly resolved) representation of the Gulf Stream and Kuroshio Current systems, and a better representation of the Loop Current in the Gulf of Mexico.

Validation of OTIS and TEOTS against independent

bathy data (i.e., unassimilated into the analyses at the time of validation) indicates that OTIS produces a more accurate representation of ocean thermal structure than TEOTS. Apparent rms errors for OTIS are generally less than those for TEOTS, particularly below about 100–150 m depth. The 0–300 m depth-averaged apparent rms errors, calculated from a 90-day accumulation of data and averaged over all areas to produce a sample size of 9980 bathy reports, show OTIS with a 7% improvement over TEOTS. The 0–300 m depth-averaged grid-scale rms errors, estimated via a technique to remove the effect of observational noise from the statistics and averaged over all areas, show OTIS with a 20% improvement over TEOTS.

OTIS was designated as the Navy's new operational global-scale ocean thermal analysis in July 1988. Present and future work involves the application of a new and more sophisticated version of OTIS on eddy-resolving regional grids, and the continued monitoring of verification statistics derived from independent bathy data.

Acknowledgments. The authors acknowledge the contributions of the following people who worked on various stages of the development and implementation of the OTIS software: Ms. Bonnie Samuels, Mr. George Innis, Mr. Bruce Mendenhall, Ms. Mary-Lou Morris, Mr. Harry Hamilton, and Ms. Charlene Dimiceli.

APPENDIX A

Definition of Symbols

A_k	Inverse of east–west decorrelation scale of resolvable thermal anomalies at gridpoint k .	T_k^c	Climatological temperature at gridpoint k .
B_k	Inverse of north–south decorrelation scale of resolvable thermal anomalies at gridpoint k .	T_i^o	Observed temperature at location i .
C_k	Inverse of temporal decorrelation scale of resolvable thermal anomalies at gridpoint k .	T_k^p	TOPS predicted temperature at gridpoint k .
e	Mean of instrumental error (i.e., bias) for MCSST observations.	z	Depth, measured positive downward from the surface in meters.
G_k	Rms TOPS error growth over one forecast cycle at gridpoint k .	z_H	Deepest reported depth in a bathy observation.
h_k^a	Analyzed mixed-layer depth at location i .	τ_j	Individual MCSST observation at location j .
h_k^c	Climatological mixed-layer depth at gridpoint k .	α_{ki}	Weight given to observation i assimilated at gridpoint k .
h_i^p	Observed mixed-layer depth at gridpoint k .	β_k	Weight given to TOPS prediction at gridpoint k .
M	Number of MCSST observations averaged around a gridpoint to form a super-observation.	γ_k	Weight given to climatology at gridpoint k .
N	Number of observations assimilated at gridpoint k .	η_{ij}	Correlation between resolvable thermal anomalies at location i and location j in space-time.
T	Temperature.	λ_i^o	Noise-to-signal ratio for observation i .
T'	Reference climatological SST gradient.	λ_k^p	Noise-to-signal ratio for TOPS prediction at gridpoint k .
T_k^a	Analyzed temperature at gridpoint k .	λ_i^p	Noise-to-signal ratio for subgrid-scale error at location i .
		λ_{av}^p	Average of λ_i^p over entire horizontal analysis domain.
		ΔX	Reference grid space.
		Δx_{ij}	East–west distance between location i and location j .
		Δy_{ij}	North–south distance between location i and location j .
		Δt_{ij}	Time difference between observation i and observation j .
		$(\Delta T_k^p)_n$	Change in TOPS predicted temperature from level $n - 1$ to level n (level 0 implies the surface) at gridpoint k .
		σ_i^o	Rms observational error of observation i .
		σ_k^p	Rms error of TOPS prediction at gridpoint k .
		σ_i^f	Long-term rms variation of resolvable thermal anomalies about climatology at location i .
		σ_i^b	Rms difference between bathy observations and climatology at location i .
		σ_{av}^b	Rms difference between bathy observations and climatology calculated over entire horizontal analysis domain.
		σ_k^v	Expected rms temperature difference between T_k^a and independent bathy observations.
		σ_i^p	Rms subgrid-scale error at location i .
		σ_i^f	Rms error added to MCSST super-observation as a result of the way in which the block averaging of the MCSST data is done.
		σ_k^a	Rms error of resolvable thermal field in resulting analysis at gridpoint k .
		$(\sigma_k^a)_{\text{INITIAL}}$	Rms error of the resolvable thermal field from the previous analysis initializing TOPS at gridpoint k .

- $(\sigma_i^o)_{EX}$ Rms error added to i th bathy observation below depth z_B by the downward extrapolation of the bathy.
- ϵ Standard deviation of instrumental error for MCSST, SHIP, or BATHY observations.

REFERENCES

- Alaka, M. A., and R. C. Elvander, 1972: Optimum interpolation from observations of mixed quality. *Mon. Wea. Rev.*, **100**, 612-624.
- Bengtsson, L., and N. Gustafsson, 1972: Assimilation of non-synoptic observations. *Tellus*, **24**, 383-399.
- Bernstein, R. L., and W. B. White, 1981: Stationary and traveling mesoscale perturbations in the Kuroshio extension current. *J. Phys. Oceanogr.*, **11**, 692-704.
- Bretherton, F. P., R. E. Davis and C. B. Fandry, 1976: A technique for objective analysis and design of oceanographic experiments applied to MODE-73. *Deep-Sea Res.*, **23**, 559-582.
- Carter, E. F., and A. R. Robinson, 1987: Analysis models for the estimation of oceanic fields. *J. Atmos. Oceanic Technol.*, **4**, 49-74.
- Clancy, R. M., 1983: The effect of observational error correlations on objective analysis of ocean thermal structure. *Deep-Sea Res.*, **30**, 985-1002.
- , 1987: Real-time applied oceanography at the Navy's global center. *Mar. Technol. Soc. J.*, **21**, 33-46.
- , and K. D. Pollak, 1983: A real-time synoptic ocean thermal analysis/forecast system. *Progress in Oceanography*, **12**, Pergamon, 383-424.
- , P. A. Phoebus and K. D. Pollak, 1989: Technical description of the Optimum Thermal Interpolation System Version 1: A model for oceanographic data assimilation. NORDA Report 240, Naval Ocean Research and Development Activity, John C. Stennis Space Center, MS 39529, 37 pp.
- Climate Analysis Center, 1988: Climate Diagnostics Bulletin, Vol. 88/6, June 1988, U.S. Department of Commerce, NOAA/NWS/NMC/CAC, Code W/NMC52, World Weather Bldg., Room 605, Washington, DC 20233.
- Cummings, J. A., 1986: Water mass climatology in the NW Atlantic with application to optimal field estimation. *Trans. Amer. Geophys. Union*, **67**, 1038.
- DiMego, G., 1988: The National Meteorological Center regional analysis system. *Mon. Wea. Rev.*, **116**, 977-1000.
- , P. Phoebus and J. McDonald, 1985: Data processing and quality control for optimum interpolation analyses at the National Meteorological Center. NMC Office Note 306, National Meteorological Center, Washington, D.C. 20233, 30 pp.
- Earle, M. D., 1985: Statistical comparisons of ship and buoy marine observations. Tech. Rep. MEC-85-8, MEC Systems Corporation, 10629 Crestwood Drive, Manassas, VA 22110, 289 pp.
- Freeland, H. J., and W. J. Gould, 1976: Objective analysis of mesoscale ocean circulation features. *Deep-Sea Res.*, **23**, 915-923.
- Gandin, L. S., 1965: Objective analysis of meteorological fields. Israel Program for Scientific Translations, Jerusalem, 242 pp.
- Hawkins, J. D., J. H. Harding, J. R. Chase, R. M. Clancy and B. L. Samuels, 1986: The impact of satellite infrared sea surface temperatures on FNOG ocean thermal analyses. NORDA Rep 142, Naval Ocean Research and Development Activity, John C. Stennis Space Center, MS 39529, 39 pp.
- Holl, M. M., M. J. Cuming and B. R. Mendenhall, 1979: The expanded ocean thermal structure analysis system: A development based on the fields by information blending methodology. Tech. Rep. M-241, Meteorology International, Inc., Monterey, CA, 216 pp.
- Hua, L. B., J. C. McWilliams and W. B. Owens, 1986: An objective analysis of the POLYMODE local dynamics experiment. Part II: Streamfunction and potential vorticity fields during the intensive period. *J. Phys. Oceanogr.*, **16**, 506-522.
- Martin, P. J., J. M. Harding, J. D. Hawkins and R. M. Clancy, 1985: The FNOG TOPS/TEOTS ocean thermal forecast/analysis system. *Navy Res. Rev.*, **37**, 3-7.
- McWilliams, J. C., 1976: Maps from the Mid-Ocean Dynamics Experiment: Part I. Geostrophic streamfunction. *J. Phys. Oceanogr.*, **6**, 810-827.
- , W. B. Owens and L. B. Hua, 1986: An objective analysis of the POLYMODE local dynamics experiment. Part I: General formalism and statistical model selection. *J. Phys. Oceanogr.*, **16**, 483-504.
- Mellor, G. L., and P. A. Durbin, 1975: The structure and dynamics of the ocean surface mixed-layer. *J. Phys. Oceanogr.*, **5**, 718-725.
- NOAA, 1988a: Oceanographic Monthly Summary, March 1988, Volume VII, No. 3, NOAA, Office of Ocean Services, Rockville, MD.
- , 1988b: Oceanographic Monthly Summary, April 1988, Volume VII, No. 4, NOAA, Office of Ocean Services, Rockville, MD.
- , 1988c: Oceanographic Monthly Summary, May 1988, Volume VII, No. 5, NOAA, Office of Ocean Services, Rockville, MD.
- Phoebus, P. A., 1988: Improvements to the data selection algorithms in the Optimum Thermal Interpolation System (OTIS). NORDA Rep. 239, Naval Ocean Research and Development Activity, John C. Stennis Space Center, MS 39529, 18 pp.
- , 1989: Quality control algorithms for ocean temperature data. NORDA Rep. 243, Naval Ocean Research and Development Activity, John C. Stennis Space Center, MS 39529.
- Reynolds, R. W., 1983: A comparison of sea surface temperature climatologies. *J. Climate Appl. Meteor.*, **22**, 447-459.
- Robinson, A. R., and W. G. Leslie, 1985: Estimation and prediction of oceanic eddy fields. *Progress in Oceanography*, **14**, Pergamon, 485-510.
- , J. A. Carton, N. Pinardi and C. N. K. Mooers, 1986: Dynamical forecasting and dynamical interpolation: An experiment in the California current. *J. Phys. Oceanogr.*, **16**, 1561-1579.
- , A. Hecht, N. Pinardi, J. Bishop, W. G. Leslie, Z. Rosentroub, A. J. Mariano and S. Brenner, 1987: Small synoptic/mesoscale eddies and energetic variability of the eastern Levantine basin. *Nature*, **327**, 131.
- Roemmich, D., 1983: Optimal estimation of hydrographic station data and derived fields. *J. Phys. Oceanogr.*, **13**, 1544-1549.
- Strong, A. E., and E. P. McClain, 1985: Improved ocean surface temperatures from space-comparison with drifting buoys. *Bull. Amer. Met. Soc.*, **65**, 138-142.
- We'gle, W. R., and B. R. Mendenhall, 1974: Climatology of the upper thermal structure of the seas. Tech. Rep. M-196, Meteorology International, Inc., Monterey, CA, 79 pp.
- White, W. B., 1977: Secular variability in the baroclinic structure of the interior North Pacific from 1950-1970. *J. Mar. Res.*, **4**, 587-607.
- , and R. L. Bernstein, 1979: Design of an oceanographic network in the midlatitude North Pacific. *J. Phys. Oceanogr.*, **9**, 592-606.